

MOL #108068

Structural Insights into the Atomistic Mechanisms of Action of Small Molecule Inhibitors Targeting the KCa3.1 Channel Pore

Hai M. Nguyen, Vikrant Singh, Brandon Pressly, David Paul Jenkins, Heike Wulff, Vladimir Yarov-Yarovoy

Department of Pharmacology (H.M.N, V.S., B.P., D.P.J., H.W.) and Department of Physiology and Membrane Biology (V. Y.-Y.), School of Medicine, University of California, Davis, California, USA

MOL #108068

Running Title: Molecular Model of Drug Binding in the K_{Ca}3.1 Pore

Address correspondence to:

Vladimir Yarov-Yarovoy, Department of Physiology and Membrane Biology, 4131 Tupper Hall, University of California, Davis, Davis, CA 95616; phone: 530-752-5298; email: yarovoy@ucdavis.edu

Heike Wulff, Department of Pharmacology, Genome and Biomedical Sciences Facility, Room 3502, 451 Health Sciences Drive, University of California, Davis, Davis, CA 95616; phone: 530-754-6136; email: hwulff@ucdavis.edu

Number of Text Pages: 39

Number of Tables: 0

Number of Figures: 9

Number of References: 80

Number of Words in the Abstract: 226

Number of Words in the Introduction: 778

Number of Words in the Discussion: 1,463

Nonstandard abbreviations used: CaM, calmodulin; DMSO, dimethyl sulfoxide; NS6180, (4-[[3-(trifluoromethyl)phenyl]methyl]-2*H*-1,4-benzothiazin-3(4*H*)-one); HEK, human embryonic kidney; K_{Ca}, Ca²⁺-activated K⁺ channel; KCa3.1, intermediate-conductance Ca²⁺-activated K⁺ channel; Kv, voltage-gated K⁺ channel; senicapoc, 2,2-bis-(4-fluorophenyl)-2-phenylacetamide; SK, small-conductance K_{Ca} channel; TRAM-7, 1-tritylpyrrolodine; TRAM-11, 1-trityl-1*H*-pyrazole; TRAM-18, 2,2,2-tris(4-methoxyphenyl)acetonitrile; TRAM-19, 1-[tris(4-methoxyphenyl)methyl]-1*H*-pyrazole; TRAM-34, 1-[(2-chlorophenyl)diphenylmethyl]-1*H*-pyrazole.

MOL #108068

Abstract

The calcium-activated potassium channel KCa3.1 constitutes an attractive pharmacological target for immunosuppression, fibroproliferative disorders, atherosclerosis and stroke. However, there currently is no available crystal structure of this medically relevant channel that could be used for structure-assisted drug design. Using the Rosetta molecular modeling suite we generated a molecular model of the KCa3.1 pore and tested the model by first confirming previously mapped binding sites and visualizing the mechanism of TRAM-34, senicapoc and NS6180 inhibition at the atomistic level. All three compounds block ion conduction directly by fully or partially occupying the site that would normally be occupied by K^+ before it enters the selectivity filter. We then challenged the model to predict the receptor sites and mechanisms of action of the dihydropyridine nifedipine and an isosteric 4-phenyl-pyran. Rosetta predicted receptor sites for nifedipine in the fenestration region and for the 4-phenyl-pyran in the pore lumen, which could both be confirmed by site-directed mutagenesis and electrophysiology. While nifedipine is thus not a pore blocker and might be stabilizing the channel in a non-conducting conformation or interfere with gating, the 4-phenyl-pyran was found to be a “classical” pore blocker that directly inhibits ion conduction similar to the triarylmethanes TRAM-34 and senicapoc. The Rosetta KCa3.1 pore model explains the mechanism of action of several KCa3.1 blockers at the molecular level and could be used for structure assisted drug design.

MOL #108068

Introduction

The intermediate-conductance Ca^{2+} -activated K^+ channel KCa3.1 (*KCNN4*) was cloned independently by three groups in 1997 from pancreas (Ishii et al., 1997), placenta (Joiner et al., 1997) or lymph node (Logsdon et al., 1997). Similar to the related small-conductance SK or KCa2 channels, KCa3.1 channels have fewer charges in their S4 segment than voltage-gated K^+ channels (Wei et al., 2005) and therefore do not respond to changes in membrane voltage, but instead are activated by Ca^{2+} binding to calmodulin, which functions as their β -subunit and induces Ca^{2+} -dependent channel opening (Fanger et al., 1999). KCa3.1 channels are accordingly able to hyperpolarize the membrane towards the K^+ equilibrium potential and modulate Ca^{2+} influx during cellular activation and proliferation by sustaining Ca^{2+} entry through Ca^{2+} -release activated Ca^{2+} (CRAC) or transient receptor potential (TRP) channels.

KCa3.1 is widely expressed in cells of the immune system such as T- and B-lymphocytes (Ghanshani et al., 2000; Wulff et al., 2004), mast cells (Shumilina et al., 2008), macrophages and microglia (Chen et al., 2015), where it plays an important role in cellular activation, migration and cytokine production (Feske et al., 2015). KCa3.1 is further important for volume regulation in erythrocytes (Vandorpe et al., 1998), which is why the channel is often referred to as the “Gárdos channel” after the Hungarian scientist, who first described a Ca^{2+} -activated K^+ efflux leading to erythrocyte dehydration in 1958 (Gardos, 1958). More recently missense mutations in KCa3.1 have been linked to hereditary stomatocytosis (xerocytosis), an autosomal dominant congenital hemolytic anemia. In addition to red and white blood cells, KCa3.1 is also expressed in dedifferentiated vascular smooth muscle cells (Kohler et al., 2003; Toyama et al., 2008), fibroblast (Pena and Rane, 1999), the vascular endothelium, where the channel is involved in the so-called endothelium-derived hyperpolarization (EDH) response (Edwards et al., 2010; Si et al., 2006), and in secretory epithelia of the lung and the gastrointestinal tract (Heitzmann and Warth, 2008), where KCa3.1 participates in fluid and

MOL #108068

electrolyte movement across the epithelium. Based on this expression pattern, KCa3.1 inhibitors constitute very attractive drug candidates for reducing inflammatory cytokine production in autoimmune disorders (Feske et al., 2015), microglia activation in stroke (Chen et al., 2015) and Alzheimer's disease (Maezawa et al., 2012), and for inhibiting smooth muscle cell and fibroblast proliferation in atherosclerosis (Toyama et al., 2008), asthma (Girodet et al., 2013), vascular restenosis (Kohler et al., 2003) and transplant rejection (Chen et al., 2013). Other potential indications for KCa3.1 inhibition are sickle cell disease (Brugnara, 2003) and secretory diarrhea in humans and farm animals (Rufo et al., 1997). Research groups in both the pharmaceutical industry and in academia have identified several classes of potent and selective KCa3.1 blockers including the triarylmethanes senicapoc (McNaughton-Smith et al., 2008) and TRAM-34 (Wulff et al., 2000), the benzothiazione NS6180 (Strobaek et al., 2013) and a series of dihydropyridine isosteric 4-phenyl-pyrans (Urbahns et al., 2003) and cyclohexadienes (Urbahns et al., 2005). Senicapoc, which was in phase-3 clinical trials for sickle cell anemia, where it failed for lack of efficacy in reducing the number of painful sickling attacks (Ataga et al., 2011), demonstrated that KCa3.1 inhibitors are safe and well tolerated in humans. However, based on issues such as short remaining patent-lives or low oral availability, none of these compounds are currently suitable for further clinical development and there is a need for identifying novel KCa3.1 inhibitors.

Since structure-based drug design approaches have not previously been attempted for KCa3.1 due to the absence of x-ray crystal structures, we here applied the Rosetta molecular modeling suite with membrane environment specific energy functions to generate structural models of the KCa3.1 pore and tested our predictions by site-directed mutagenesis and electrophysiology. Rosetta has previously been successfully used to calculate gating charges (Khalili-Araghi et al., 2010), simulate voltage-sensor movements (DeCaen et al., 2011; DeCaen et al., 2009; DeCaen et al., 2008; Tuluc et al., 2016; Yarov-Yarovoy et al., 2012), construct open and closed state conformations of voltage-gated K⁺ channels (Pathak et al., 2007; Yarov-

MOL #108068

Yarovoy et al., 2006a), or model the interactions of scorpion toxins with voltage-gated Na⁺ channels (Cestele et al., 2006; Wang et al., 2011; Zhang et al., 2011; 2012). More recently, Rosetta has been utilized to simulate the access and binding of local anesthetics and anticonvulsants to Na⁺ channels (Boiteux et al., 2014), study the interaction of capsaicin with the TRPV1 channel (Yang et al., 2015), and rationally design a vanilloid-sensitive TRPV2 channel (Yang et al., 2016). Similarly, the KCa3.1 structural models we developed in our current study accurately identified key residues for binding of several small molecule probes and explain their atomistic mechanisms of action. We propose that our models could be useful as tools for future structure-assisted KCa3.1 modulator design.

Material and Methods

RosettaMembrane modeling of the KCa3.1 channel pore-forming domain. Homology, *de novo*, and full-atom modeling of the KCa3.1 channel pore was performed using the Rosetta molecular modeling suite (Rohl et al., 2004) using membrane environment specific energy functions (Barth et al., 2007; Yarov-Yarovoy et al., 2012; Yarov-Yarovoy et al., 2006b) and loop modeling applications (Mandell et al., 2009; Wang et al., 2007). The pore-forming domain structure of the Kv1.2-Kv2.1 chimeric channel (Protein Data Bank ID: 2R9R) (Long et al., 2007) and the open KcsA structure (Protein Data Bank ID: 3FB5) (Cuello et al., 2010) were used as templates. The HHpred server (Hildebrand et al., 2009; Soding et al., 2005) based alignment between KCa3.1, Kv1.2 and KcsA used for homology modeling is shown in Figure 1. 10,000 models were generated and the 1,000 lowest energy models were clustered with a root mean square deviation (RMSD) threshold of 2.0 Å between Cα atoms. The top cluster homology

MOL #108068

models of the Kv1.2- and the KcsA-based KCa3.1 channel (from the loop modeling round) were used for docking of small molecules. All structural figures in this paper were generated using the UCSF Chimera package (Pettersen et al., 2004). Protein Data Bank (pdb) format files of all models shown in this study are available upon request.

RosettaLigand docking of small molecules to the hKCa3.1 channel. Ligand docking was performed using the RosettaLigand application (Davis and Baker, 2009; Meiler and Baker, 2006) that is comprised of three stages, which progress from low-resolution conformational sampling and scoring to full atom optimization and all-atom energy function. In the first, low-resolution stage, the ligand is placed randomly within the binding site and its "center of mass" is constrained to move within a 10 Å diameter sphere. Hundreds of ligand conformers are generated using OpenEye software (Hawkins and Nicholls, 2012; Hawkins et al., 2010) and are then randomly rotated as a rigid body and scored for shape compatibility with the target protein. The best-scoring models are filtered by RMSD to eliminate near-duplicates and one of the remaining models is selected at random to continue to the next stage. The second, high-resolution stage employs the Monte Carlo minimization protocol in which the ligand position and orientation are randomly perturbed by a small deviation (0.1 Å and 3°); receptor side chains are repacked using a rotamer library; the ligand position, orientation, and torsions and protein side-chain torsions are simultaneously optimized using quasi-Newton minimization and the end result is accepted or rejected based on the Metropolis criterion. Scoring uses the full-atom Rosetta energy function with softened van der Waals repulsion. The side-chain rotamers are searched simultaneously during "full repack" cycles and one at a time in the "rotamer trials" cycles. The full repack makes $\sim 10^6$ random rotamer substitutions at random positions and accepts or rejects each on the Metropolis criterion. Rotamer trials choose the single best rotamer at a random position in the context of the current state of the rest of the system, with the positions visited once each in random order. The ligand is treated as a single residue and its input conformers

MOL #108068

serve as rotamers during this stage. During the energy minimization step, the finely sampled rotamer library and soft-repulsive energy function allow access to off-rotamer conformations. The third and final stage is a more stringent gradient-based minimization of the ligand position, orientation, and torsions and the receptor torsions for both side chains and backbone. Scoring uses the same Rosetta energy function, but with a hard-repulsive van der Waals potential, which creates a more rugged energy landscape that is better at discriminating native from non-native binding modes. Twenty thousand docking trajectories were generated for each channel–ligand pair and the top structures were selected according to the Rosetta energy.

Site-directed mutagenesis and electrophysiology. The human wild-type KCa3.1 cDNA coding region was originally cloned in the pEGFP-C1 plasmid vector (Wulff et al., 2001). To construct the mutations, PCR-based site-directed mutagenesis was performed directly on the wild-type plasmid and the desired mutations were confirmed by sequencing. COS-7 cells were obtained from ATCC. Cells were maintained in DMEM supplemented with 10% fetal calf serum were used for expression of KCa3.1 and mutant channels using FuGENE® 6 transfection reagent (Promega, Madison, WI) in Opti-MEM® reduced serum medium (Life Technologies, Benicia, CA). Transfected cells were cultured in 24-well plates for 24 h or 48 h and were then detached by trypsinization, washed, attached to poly-L-lysine coated glass cover-slips, and then studied in the whole-cell mode of the patch-clamp technique with an EPC-10 HEKA amplifier. Patch pipettes were pulled from soda lime glass micro-hematocrit tubes (Kimble Chase, Rochester, NY) to resistances of 2-3 M Ω to achieve good access and efficient and complete cell dialysis for internals with high free Ca²⁺ concentrations. The pipette solution contained 145 mM K⁺ aspartate, 2 mM MgCl₂, 10 mM HEPES, 10 mM K₂EGTA and 8.5 mM CaCl₂ (1 μ M free Ca²⁺), pH 7.2, 290 mOsm. To reduce chloride “leak” currents endogenous to COS-7 cells, which can contaminate the K⁺ current at depolarized potentials, we used a Na⁺ aspartate external solution

MOL #108068

containing 160 mM Na⁺ aspartate, 4.5 mM KCl, 2 CaCl₂, 1 mM MgCl₂, 5 mM HEPES, pH 7.4, 300 mOsm. K⁺ currents were elicited with voltage ramps from -120 to 40 mV of 200-ms duration applied every 10 s. Whole-cell K_{Ca}3.1 current amplitude was measured at 40 mV in control external solution or inhibitor-containing external solutions. TRAM-34, nifedipine and 4-phenyl-puran stocks were prepared in DMSO and drug dilutions were freshly prepared before each recording. Data analysis was performed using IgorPro (WaveMetrics, Inc.) or Microsoft Excel (Microsoft). Concentration-response curve fitting to the Hill equation to obtain IC₅₀ values and Hill coefficients was performed with Origin 9.0 (OriginLab). All data are expressed as mean ± SD.

MOL #108068

Results

Atomistic structural model of the KCa3.1 pore domain

We applied Rosetta modeling to study the molecular mechanism of action of multiple small molecules interacting with multiple receptor sites within the KCa3.1 channel pore. Out of the available open state K⁺ channel structures, such as KcsA, MthK, KvAP, and Kv1.2, we chose the Kv1.2 channel x-ray crystal structure (Long et al., 2007) as a template for homology modeling, because several of the compounds used in our study cross-react to Kv1.2 at higher concentrations (Strobaek et al., 2013; Wulff et al., 2000). To begin with, we build a homology model of the human KCa3.1 channel pore-forming domain (PD) as described in the Methods. Due to significant sequence differences between KCa3.1 and Kv1.2 channels in the loop between S5 and the P helix in the selectivity filter region (Fig. 1), we predicted the structure of this loop *de novo*. The most frequently sampled and lowest energy KCa3.1 channel models have converged on the model presented in Fig. 2A-D. Key residues forming possible receptor sites for small molecule drugs in our study are positioned within the pore lumen or fenestration regions of the KCa3.1 pore structure (Fig. 2D).

However, because the Kv1.2 channel contains a proline-valine-proline sequence motif that forms a bend in the S6 helix and therefore might not be the most appropriate template for the corresponding leucine-valine-alanine sequence in KCa3.1 despite the similarities in pharmacology between KCa3.1 and Kv1.2, we also built a second KCa3.1 pore model using the KcsA structure in an open-conductive state (Cuello et al., 2010) as a template (Fig. 3). The KcsA based KCa3.1 model reveals a relatively smaller pore lumen volume compared to the Kv1.2 based KCa3.1 model (Fig. 3C), which originates from differences in relative positions of the pore lining helices in the original KcsA and Kv1.2 structures.

MOL #108068

Model of the triarylmethane receptor site in the pore lumen

Based on mutagenesis studies the pore lumen of KCa3.1 is known to be the target for both triarylmethane-type KCa3.1 blockers like clotrimazole and TRAM-34 as well as the benzothiazinone NS6180 (Strobaek et al., 2013; Wulff et al., 2001). Both TRAM-34 and NS6180 inhibit KCa3.1 with similar potencies (IC_{50} 10-20 nM) and are 200-1000-fold selective over other voltage-gated cation channels (Strobaek et al., 2013). Our Kv1.2-based open state KCa3.1 model (Fig. 4) shows that the side chains of T250 (in the selectivity filter region) and V275 (in transmembrane segment S6) project directly towards the pore lumen environment and are in a position to potentially interact with small molecule blockers. We used the RosettaLigand application, which has been developed by Jens Meiler's and David Baker's groups to predict small molecule – protein interactions (Davis and Baker, 2009; Davis et al., 2009; DeLuca et al., 2015; Lemmon and Meiler, 2013; Meiler and Baker, 2006; Tinberg et al., 2013), to generate preliminary models of TRAM-34 (Fig. 4), several other structurally related triarylmethanes (Fig. 5), and NS6180 (Fig. 6) binding to KCa3.1 in an open state as described in the Methods.

TRAM-34 was placed into 20,000 random starting positions in the outer vestibule, the fenestration region and the inner pore. While minimization in the outer vestibule or the fenestration region did not converge on any energetically favorable binding poses (Supplemental Fig. 1), TRAM-34 converged in the pore. Our most energetically favorable model of the KCa3.1-TRAM-34 complex suggests that TRAM-34 interacts with T250 and V275 in the pore-lumen (Fig. 4A, 4B, 4C), two residues that have previously been shown to completely abolish triarylmethane sensitivity when mutated to the corresponding residues in KCa2.3 (T250S and V275A), which is not sensitive to TRAM-34 (Wulff et al., 2001). Conversely, introduction of T and V into the corresponding positions in KCa2.3 renders this channel sensitive to triarylmethanes (Wulff et al., 2001). The T250 side chain in each subunit forms part of the ion binding site in the potassium channel selectivity filter (Zhou et al., 2001). Based on our model, TRAM-34 is situated near the T250 side chains from all 4 subunits and blocks ion

MOL #108068

conduction directly by occupying the site that would normally be occupied by potassium before it enters the selectivity filter. The pyrazole ring of TRAM-34 is positioned between the V275 side chains from adjacent subunits with the pyrazole nitrogen forming a hydrogen bond with the T250 side-chain from one of the subunits (Fig. 4A, 4B and 4C). In contrast to the Kv1.2-based KCa3.1 model, TRAM-34 failed to converge in the KcsA-based KCa3.1 model (Supplemental Fig. 2). We suggest that the narrower pore lumen below the selectivity filter in the KcsA-based KCa3.1 model (Fig. 3C) does not allow shape complementarity between TRAM-34 and its receptor site near V275 and formation of a hydrogen bond with T250.

The binding orientation of TRAM-34 in the Kv1.2-based KCa3.1 model agrees well with the structure activity relationship observations that were previously made when testing 83 triarylmethanes (Wulff et al., 2000). TRAM-34's pyrazole ring could be replaced by other hydrogen bond accepting heterocycles such as imidazole or tetrazole but not by pyrrole or other substituents lacking a hydrogen bond acceptor without at least a 500-fold drop in potency. The molecular dimensions of the binding site are also in line with our previous estimation of the molecular dimensions of the triarylmethane pharmacophore (Wulff et al., 2000) of roughly 9.5 Å by 9.5 Å by 8.6 Å. In order to determine if the Rosetta KCa3.1 pore model would support these structure activity relationships we docked a sample set of triarylmethanes (Fig. 5E) consisting of the high affinity blocker senicapoc (IC_{50} 11 nM), TRAM-7 and TRAM-11, two compounds blocking KCa3.1 with micromolar affinity, and two inactive compounds, TRAM-18 and TRAM-19 (Wulff et al., 2000). For senicapoc the 50 lowest energy binding poses all showed two hydrogen bonds between the amino-group of the ligand and the oxygen atoms of the hydroxyl groups of T250 residues from adjacent subunits (Fig. 5A). Similar to TRAM-34 (black in Fig. 5B), senicapoc (orange in Fig. 5B) is occupying the potassium binding site below the selectivity filter and is thus physically obstructing permeation. However, instead of acting as a hydrogen bond acceptor, senicapoc acts as a hydrogen bond donor (Fig. 5B). For the less potent TRAM-11 (IC_{50} 2.5 μ M) Rosetta converged on two preferred binding poses that both show this compound

MOL #108068

lower down in the cavity, where despite having the same pyrazole substituent as TRAM-34, that could theoretically form a hydrogen bond with the T250 side chain, it is out of range for a hydrogen bond (~ 2.1 Å) with T250 and is instead forming a hydrogen bond with T278 (Fig. 5D) and rotating around this hydrogen bond in its different poses. Unfortunately, we could not confirm this binding pose experimentally. Mutating T278 to alanine and valine resulted in non-functional channels, while mutating T278 to a large, aromatic phenylalanine did not significantly change TRAM-11 activity (see Supplemental Data). Rosetta modeling of the T278F mutant explained these somewhat puzzling results by showing 278F facing away from the cavity and TRAM-11 positioned “higher up” now forming a hydrogen bond with T250 (Supplemental Fig. 3). TRAM-7, a triarylmethane blocking KCa3.1 around 20 μ M, and which is missing the chloro-substituent and bearing an aliphatic pyrrolidine ring instead of TRAM-34’s pyrazole ring, also was modeled lower down in the cavity by Rosetta (Fig. 5C), where it rotated around itself without forming any detectable hydrogen bonds or other stable interactions. Interestingly, when either one of the two inactive TRAMs, TRAM-18 or TRAM-19 (Fig. 5E), were energy minimized in the pore lumen, Rosetta did not converge on any particular binding pose and the compounds were often ejected from the cavity during energy minimization in keeping with their experimentally observed inability to block KCa3.1.

We also generated a structural model of the benzothiazinone NS6180 (Fig. 6), another small molecule that has been shown by electrophysiology and site directed mutagenesis to interact with T250 and V275 in the KCa3.1 pore lumen (Strobaek et al., 2013). In contrast to TRAM-34, which is positioned directly under the selectivity filter region and interacts with residues from all four subunits, NS6180 interacts with the T250 and V275 side chains from only two adjacent subunits and its elongated structure is oriented along the S6 helices (Fig. 6A, 6B, 6C). Based on this model, we suggest that NS6180, although “sitting” differently from TRAM-34, blocks potassium conduction in a similar fashion, namely by overlapping with the potassium binding site within the pore lumen (Zhou et al., 2001) and thus preventing ion permeation. This binding

MOL #108068

model is in agreement with electrophysiological experiments showing that TRAM-34 and NS6180 have nearly identical potencies and are very hard to wash out (Strobaek et al., 2013).

Structural modeling of the unknown KCa3.1 binding site of the dihydropyridine nifedipine

In order to be useful for structure assisted design efforts, a model should also be able to correctly predict binding site locations and molecular mechanism of action of small molecules that have not been previously mapped by electrophysiology and site directed mutagenesis. We therefore decided to “challenge” the KCa3.1 pore model with two compounds whose binding sites are unidentified. Nifedipine, which is a potent calcium channel blocker, has long been known to also inhibit KCa3.1 at low micromolar concentrations (Jensen et al., 1998; Wulff et al., 2001). It more recently served as template for medicinal chemists at Bayer who isosterically replaced the N in the dihydropyridine ring with an O or C atom and generated several phenylpyrans (Urbahns et al., 2003) and cyclohexadienes (Urbahns et al., 2005), which inhibit KCa3.1 at low nanomolar concentrations without affecting L-type calcium channels. We used the RosettaLigand method to generate structural models of nifedipine binding to the KCa3.1 pore lumen and fenestration regions. Modeling of nifedipine to the pore lumen region did not converge on any particular model (data not shown) in agreement with the finding that the T250S-V275A double mutant in the pore lumen does not reduce the potency of nifedipine inhibition of KCa3.1 but rather enhances nifedipine activity (Fig. 7E-H). In contrast, modeling of nifedipine to the fenestration region converged on three groups of models with the most frequently sampled binding pose of the drug shown in Fig. 7. This model suggests that nifedipine may fit within the fenestration of the KCa3.1 pore between the side-chains of T212 (in S5) and V272 (in S6) from adjacent subunits (Fig. 7A, 7B, 7C) and could be stabilizing the channel in a non-conducting conformation without directly occluding the pore.

We tested this prediction by mutating T212 and V272 to phenylalanine reasoning that the bulky phenylalanine side-chains will overlap and close-off the fenestration binding site for

MOL #108068

nifedipine and thus reduce its affinity to the channel. The T212F and T272F single mutants reduced nifedipine's IC_{50} approximately 4- and 8-fold, respectively (Fig. 7E), while the T212F-V272F double mutant reduced the IC_{50} 14-fold (Fig. 7E). Interestingly, all three fenestration mutants retained the same high sensitivity to TRAM-34 (IC_{50} ~20 nM) as the wild-type KCa3.1 channel suggesting that the mutations had not significantly altered the pore lumen structure (Fig. 7I).

Structural modeling of the unknown binding sites of a 4-phenyl-pyran

We next resynthesized an exemplary 4-phenyl-pyran from the Bayer KCa3.1 work (Urbahns et al., 2003) using an alternative synthetic route (see Supplemental Data) since we wanted to further probe the KCa3.1 model with a more potent nifedipine derivative. In electrophysiological experiments we found that the 4-phenyl-pyran **3** blocked KCa3.1 current with an IC_{50} of 7.7 nM (Fig. 8E), which is in agreement with the previously reported IC_{50} of 8 nM (Urbahns et al., 2003). Based on the structural similarity between nifedipine and the 4-phenyl-pyran we expected that this compound would also bind in the fenestration region. However, to our surprise, we found that the RosettaLigand method failed to converge on any energetically favorable binding pose for the *R* enantiomer of the 4-phenyl-pyran in the fenestration region and only predicted one hydrogen bonding interaction with threonine 212 for the *S* enantiomer. In contrast, modeling of both the (*S*)- and (*R*)-4-phenyl-pyran in the inner pore converged on the very energetically favorable binding pose shown for the *S* enantiomer in Fig. 8A-D and for the *R* enantiomer in Fig. 9. Both the (*S*)- and (*R*)-4-phenyl-pyran are positioned near the side chains of T250 in the selectivity filter region, of V275 in S6, and of T278 in S6 from three adjacent subunits and block ion conduction directly by undergoing three hydrogen bonds and three van der Waals interactions. Subsequent electrophysiological experiments with the fenestration mutants confirmed this prediction and showed that the V272F and V212F-V272V mutants were still remarkably sensitive (IC_{50S} ~ 30 nM), while mutations in the pore lumen dramatically reduced

MOL #108068

potency with the T250S-V275A mutant being more than 500-fold less sensitive ($IC_{50} \sim 4.4 \mu\text{M}$). The T250 side chains from two adjacent subunits form hydrogen bonds with the carbonyl-oxygen of the acetyl substituent in 3-position of the pyran ring (Fig. 8A, 8C), while T278 from one of the subunits forms a hydrogen bond with the carbonyl-oxygen of the methyl-ester in 5-position (Fig. 8A, 8C). This observation is in agreement with the finding that mutating T278 to phenylalanine reduced the IC_{50} by 40-fold. Additionally, V275 side chains from three adjacent subunits have van der Waals interactions with the (*S*)-4-phenyl-pyran (Fig. 8B, 8C). The para-chloro atom on the phenyl ring of the 4-phenyl-pyran system is positioned between side chains of T278 and A279 in S6 (Fig. 8B), while the meta- CF_3 group is oriented down towards the intracellular side of the membrane (Fig. 8C). The (*R*)-enantiomer is “flipped” but is undergoing the same interactions with T250, V275 and T278 from different subunits because of the overall symmetry of the tetrameric channel (Fig. 9). Overall, this binding orientation of the 4-phenyl-pyran and the contacts it is making to the channel through its two carbonyl oxygens, and the chloro- and trifluoromethyl substituents on the phenyl ring, are consistent with the published structure activity relationship findings that these four moieties are essential for high potency KCa3.1 inhibition in the phenyl-pyran series of compounds (Urbahns et al., 2003).

MOL #108068

Discussion

Using the Rosetta molecular modeling suite we generated a molecular model of the pore domain of the calcium-activated K⁺ channel KCa3.1 and tested the model by first confirming previously mapped binding sites and visualizing the mechanism of TRAM-34, senicapoc and NS6180 inhibition at the atomistic level. All three compounds block ion conduction directly by fully or partially occupying the site that would normally be occupied by K⁺ before it enters the selectivity filter. We then tested if our KCa3.1 model would be useful for predicting the previously unknown binding sites of nifedipine and the isosteric 4-phenyl-pyran. Rosetta predicted receptor sites for nifedipine in the fenestration region and for the 4-phenyl-pyran in the pore lumen, which could both be confirmed by site-directed mutagenesis and electrophysiology. While nifedipine is thus not a pore blocker and might be stabilizing the channel in a non-conducting conformation or interfere with gating, the 4-phenyl-pyran was found to be a “classical” pore blocker that directly inhibits ion conduction similar to the triarylmethanes TRAM-34 and senicapoc.

The Kv1.2 channel structure (Long et al., 2007) was one of several possible templates for homology modeling of the KCa3.1 channel pore. Of the other available open state K⁺ channel structures, such as MthK (Jiang et al., 2002), KvAP (Jiang et al., 2003), and KcsA (Cuello et al., 2010), we also explored the open-conductive state KcsA structure here and found it an inferior template since the high affinity inner pore blocker TRAM-34 failed to converge in the KcsA-based KCa3.1 pore model. We therefore believe that based on the overall 27% sequence identity between KCa3.1 and Kv1.2 in the pore domain and the similarities in pharmacology, Kv1.2 is the most appropriate available template in the absence of a *bona-fide* KCa3.1 structure. Several venom peptides such as charybdotoxin and maurotoxin inhibit both Kv1.2 and KCa3.1 with similar potencies (Castle et al., 2003; Sprunger et al., 1996) suggesting similarities in the outer vestibule. Similarly, several of the small molecule KCa3.1 blockers used in this study such as TRAM-34 and NS6180 inhibit Kv1.2 at low micromolar concentrations (Strobaek

MOL #108068

et al., 2013; Wulff et al., 2000) again suggesting that Kv1.2 is a better template than the bacterial channels despite the fact that the proline-valine-proline sequence in the Kv1.2 channel S6 segments creates a significant bend downstream of the small molecule binding site in the inner pore that is unlikely to be present in the KCa3.1 channel structure. Another possible template would have been the recently solved structure of the sodium-activated K⁺ channel Slo2.2 in the closed state (Hite et al., 2015). However, although initially being classified as a KCa channel (KCa4.1), this channel has only 7% sequence identity to KCa1.1 (BK) and even less to KCa3.1 and has therefore just been renamed as KNa1.2 according to the new IUPHAR nomenclature (Alexander et al., 2015). The channel is also insensitive to both TRAM-34 and NS6180 (Strobaek et al., 2013) making it an unattractive template.

Our new Rosetta model of the open state conformation of the KCa3.1 channel pore correctly identified T250 and V275, two residues previously suggested based on mutagenesis to form the triarylmethane (TRAM-34 and senicapoc) and benzothiazinone (NS6180) receptor sites, as key interacting residues. Although these findings are confirmatory in nature, the atomistic models provide new insights into the orientation and the chemical nature of the interactions of the two ligands with KCa3.1. While TRAM-34 is “sitting” directly under the selectivity filter with its pyrazole positioned between the V275 side chains from adjacent subunits and the pyrazole nitrogen forming a hydrogen bond with the T250 side-chain from one of the subunits, NS6180 is oriented along S6 interacting with the T250 and V275 side chains from only two adjacent subunits. It should also be mentioned here that an older KCa3.1 pore model, which had been built to model the interaction of charybdotoxin with the KCa3.1 pore (Rauer et al., 1999) and which was based on the closed KcsA structure (Doyle et al., 1998), did not provide enough space in the inner pore to accommodate TRAM-34 and related triarylmethanes. As shown in this study, our new KCa3.1 model based on the open Kv1.2 structure, now easily accommodates TRAM-34 and other triarylmethanes like senicapoc (Fig. 4) in the inner cavity and is in agreement with our own previously performed mutagenesis studies (Strobaek et al.,

MOL #108068

2013; Wulff et al., 2001). Other less potent triarylmethanes were modeled with binding poses lower down in the cavity, where they were not in a position to effectively prevent K⁺ permeation, while inactive compounds did not converge and were ejected from the cavity during energy minimization.

In addition to the inner pore lumen, which contains the binding sites for TRAM-34 and NS6180, we identified the fenestration region in the KCa3.1 channel model as a key binding site for nifedipine in this study (see Fig. 7). This suggests a possible mechanism of KCa3.1 inhibition by nifedipine via stabilizing the channel in a non-conducting conformation without directly occluding the pore. The presence of nifedipine in the fenestration could for example allosterically affect the selectivity filter similar to what has recently been reported in a crystallographic study for the binding of several dihydropyridines to the homotetrameric Ca_vAb channel, a model for voltage-gated Ca²⁺ channels (Tang et al., 2016). The presence of one dihydropyridine molecule in the lipid-facing interface between two subunits was sufficient to induce an asymmetric, non-conducting conformation in the selectivity filter of the channel (Tang et al., 2016). Alternatively, the nifedipine molecule in the fenestration could prevent the gating movement that is translated from the C-terminal calmodulin to the gate, which for KCa3.1 has been proposed to be located at the level of the selectivity filter (Garneau et al., 2014; Klein et al., 2007). Since the T212F-V272F double mutant significantly reduced nifedipine binding, but did not eliminate it completely, we think it possible that the fenestration region may be a dynamic part of the KCa3.1 channel structure and adopt conformations that may allow low affinity nifedipine binding. It would of course also be possible that similar to Ca_vAb (Tang et al., 2016), KCa3.1 has a second, lower affinity binding site for dihydropyridines in the inner cavity, which would be in line with the observation that the T250S-V275A mutant is 4.5-fold more sensitive to nifedipine than the wild-type channel.

One very interesting and in some ways unexpected observation from our study was that the nifedipine isosteric 4-phenyl-pyran is not binding to the same site in KCa3.1 and does not have

MOL #108068

the same atomistic mechanism of action as its template nifedipine. Medicinal chemists generally assume when they make isosteric replacements in order to improve potency and selectivity that the template and the derivatives bind to the same site when deducing structure-activity-relationships (SAR). This is clearly not the case here and the findings certainly surprised us. However, the pore lumen binding site for the 4-phenyl-pyran that accommodates both the *S* and the *R* enantiomer is perfectly consistent with the published SAR of the phenyl-pyrans (Urbahns et al., 2003) and carba-analogous cyclohexadienes (Urbahns et al., 2005) and the fact that racemic compounds in these two series are equally or more potent than structurally closely related non-racemic compounds. In our model there is no contact to the pyran ring O (which was NH in nifedipine and is a simple aliphatic carbon in the equally potent cyclohexadienes), while the carbonyl groups of the ester and acetyl substituents are stabilized by hydrogen bonds in keeping with the observation that the presence and a relatively small size of the ester or acetyl side chains in 3- and 5- position is absolutely required for high potency KCa3.1 inhibition (Urbahns et al., 2005; Urbahns et al., 2003). Our model further provides an explanation for the observation that para-chloro and meta-CF₃ is the optimal substitution of the 4-phenyl-pyran system by showing van der Waals interactions between T278 and A279 and the Cl atom and the bulky, lipophilic CF₃ group.

Structure-based or structure-assisted design of ion channel modulators has long been a challenging endeavor. The field has recently advanced greatly with the increasing availability of both x-ray and cryo-EM crystal ion channel structures. However, cryo-EM structures resolution does not reveal atomistic details of small molecule – channel interactions and there still is an urgent need for co-crystals of medically relevant ion channels with small molecule drugs to truly enable structure based drug design. This knowledge gap can be bridged by computational modeling approaches like the Rosetta molecular modeling suite with membrane environment specific energy function. Our study has shown that Rosetta can generate atomistic models of small molecule - channel interactions that 1) confirm previously mapped binding sites, 2)

MOL #108068

accurately predict unknown binding sites, 3) suggest molecular mechanisms of small molecule action, and 4) explain structure-activity relationships for compounds belonging to different structural classes and binding to different sites in the pore domain.

Authorship Contributions

Participated in research design: Hai M. Nguyen, Heike Wulff, Vladimir Yarov-Yarovoy

Conducted patch-clamp recordings and data analysis: Hai M. Nguyen, David P. Jenkins,

Performed molecular modeling and related data analysis: Brandon Pressly, Vladimir Yarov-Yarovoy

Synthesized 4-phenyl-pyran: Vikrant Singh

Wrote or contributed to the writing of the manuscript: Hai M. Nguyen, Brandon Pressly, Heike Wulff, Vladimir Yarov-Yarovoy

MOL #108068

References

Alexander SP, Kelly E, Marrion N, Peters JA, Benson HE, Faccenda E, Pawson AJ, Sharman JL, Southan C, Buneman OP, Catterall WA, Cidlowski JA, Davenport AP, Fabbro D, Fan G, McGrath JC, Spedding M, Davies JA, Collaborators C (2015) The Concise Guide to PHARMACOLOGY 2015/16: Overview. *Br J Pharmacol* **172**: 5729-5743.

Ataga KI, Reid M, Ballas SK, Yasin Z, Bigelow C, James LS, Smith WR, Galacteros F, Kutlar A, Hull JH, Stocker JW (2011) Improvements in haemolysis and indicators of erythrocyte survival do not correlate with acute vaso-occlusive crises in patients with sickle cell disease: a phase III randomized, placebo-controlled, double-blind study of the Gardos channel blocker senicapoc (ICA-17043). *Br J Haematol* **153**: 92-104.

Barth P, Schonbrun J, Baker D (2007) Toward high-resolution prediction and design of transmembrane helical protein structures. *Proc Natl Acad Sci USA* **104**: 15682-15687.

Boiteux C, Vorobyov I, French RJ, French C, Yarov-Yarovoy V, Allen TW (2014) Local anesthetic and antiepileptic drug access and binding to a bacterial voltage-gated sodium channel. *Proc Natl Acad Sci USA* **111**: 13057-13062.

Brugnara C (2003) Sickle cell disease: from membrane pathophysiology to novel therapies for prevention of erythrocyte dehydration. *J Pediatr Hematol Oncol* **25**: 927-933.

Castle NA, Lodon DO, Creech C, Fajloun Z, Stocker JW, Sabatier J-M (2003) Maurotoxin - a potent inhibitor of the intermediate conductance Ca^{2+} -activated potassium channel. *Mol Pharmacol* **63**: 409-418.

MOL #108068

Cestele S, Yarov-Yarovoy V, Qu Y, Sampieri F, Scheuer T, Catterall WA (2006) Structure and function of the voltage sensor of sodium channels probed by a beta-scorpion toxin. *J Biol Chem* **281**: 21332-21344.

Chen YJ, Lam J, Gregory CR, Schrepfer S, Wulff H (2013) The Ca²⁺-activated K⁺ channel KCa3.1 as a potential new target for the prevention of allograft vasculopathy. *PloS One* **8**: e81006.

Chen YJ, Nguyen HM, Maezawa I, Grössinger EM, Garing AL, Kohler R, Jin LW, Wulff H (2016) The potassium channel KCa3.1 constitutes a pharmacological target for neuroinflammation associated with ischemia/reperfusion stroke. *J Cereb Blood Flow Metab* **36**: 2146-2161.

Clamp M, Cuff J, Searle SM, Barton GJ (2004) The Jalview Java alignment editor. *Bioinformatics* **20**: 426-427.

Clamp ME, Cuff, J. A. and Barton, G. J. (1999) Jalview- a java multiple sequence alignment viewer and editor. <http://www.ebi.ac.uk/~michele/jalview>.

Cuello LG, Jogini V, Cortes DM, Pan AC, Gagnon DG, Dalmas O, Cordero-Morales JF, Chakrapani S, Roux B, Perozo E (2010). Structural basis for the coupling between activation and inactivation gates in K⁺ channels. *Nature* **466**: 272-275.

Davis IW, Baker D (2009a). RosettaLigand docking with full ligand and receptor flexibility. *J Mol Biol* **385**: 381-392.

MOL #108068

Davis IW, Raha K, Head MS, Baker D (2009b) Blind docking of pharmaceutically relevant compounds using RosettaLigand. *Protein Sci* **18**: 1998-2002.

DeCaen PG, Yarov-Yarovoy V, Scheuer T, Catterall WA (2011) Gating charge interactions with the S1 segment during activation of a Na⁺ channel voltage sensor. *Proc Natl Acad Sci USA* **108**: 18825-18830.

DeCaen PG, Yarov-Yarovoy V, Sharp EM, Scheuer T, Catterall WA (2009) Sequential formation of ion pairs during activation of a sodium channel voltage sensor. *Proc Natl Acad Sci USA* **106**: 22498-22503.

DeCaen PG, Yarov-Yarovoy V, Zhao Y, Scheuer T, Catterall WA (2008) Disulfide locking a sodium channel voltage sensor reveals ion pair formation during activation. *Proc Natl Acad Sci USA* **105**: 15142-15147.

DeLuca S, Khar K, Meiler J (2015) Fully flexible docking of medium sized ligand libraries with RosettaLigand. *PloS One* **10**: e0132508.

Doyle DA, Morais Cabral J, Pfuetzner RA, Kuo A, Gulbis JM, Cohen SL, Chait BT, MacKinnon R (1998) The structure of the potassium channel: molecular basis of K⁺ conduction and selectivity. *Science* **280**: 69-77.

Edwards G, Feletou M, Weston AH (2010) Endothelium-derived hyperpolarising factors and associated pathways: a synopsis. *Pflugers Arch* **459**: 863-879.

MOL #108068

Fanger CM, Ghanshani S, Logsdon NJ, Rauer H, Kalman K, Zhou J, Beckingham K, Chandy KG, Cahalan MD, Aiyar J (1999) Calmodulin mediates calcium-dependent activation of the intermediate conductance KCa channel, IKCa1. *J Biol Chem* **274**: 5746-5754.

Feske S, Wulff H, Skolnik EY (2015) Ion channels in innate and adaptive immunity. *Ann Rev Immunol* **33**: 291-353.

Gardos G (1958) The function of calcium in the potassium permeability of human erythrocytes. *Biochem Biophys Acta* **30**: 653-654.

Garneau L, Klein H, Lavoie MF, Brochiero E, Parent L, Sauve R (2014) Aromatic-aromatic interactions between residues in KCa3.1 pore helix and S5 transmembrane segment control the channel gating process. *J Gen Physiol* **143**: 289-307.

Ghanshani S, Wulff H, Miller MJ, Rohm H, Neben A, Gutman GA, Cahalan MD, Chandy KG (2000) Up-regulation of the IKCa1 potassium channel during T-cell activation. Molecular mechanism and functional consequences. *J Biol Chem* **275**: 37137-37149.

Girodet PO, Ozier A, Carvalho G, Ilina O, Ousova O, Gadeau AP, Begueret H, Wulff H, Marthan R, Bradding P, Berger P (2013) Ca²⁺-activated K⁺ channel-3.1 blocker TRAM-34 attenuates airway remodeling and eosinophilia in a murine asthma model. *Am J Respir Cell Mol Biol* **48**: 212-219.

Hawkins PC, Nicholls A (2012) Conformer generation with OMEGA: learning from the data set and the analysis of failures. *J Chem Inf Model* **52**: 2919-2936.

MOL #108068

Hawkins PC, Skillman AG, Warren GL, Ellingson BA, Stahl MT (2010) Conformer generation with OMEGA: algorithm and validation using high quality structures from the Protein Databank and Cambridge Structural Database. *J Chem Inf Model* **50**: 572-584.

Heitzmann D, Warth R (2008) Physiology and pathophysiology of potassium channels in gastrointestinal epithelia. *Physiol Rev* **88**: 1119-1182.

Hildebrand A, Remmert M, Biegert A, Soding J (2009) Fast and accurate automatic structure prediction with HHpred. *Proteins* 77 Suppl **9**: 128-132.

Hite RK, Yuan P, Li Z, Hsuing Y, Walz T, MacKinnon R (2015) Cryo-electron microscopy structure of the Slo2.2 Na⁺-activated K⁺ channel. *Nature* **527**: 198-203.

Ishii TM, Silvia C, Hirschberg B, Bond CT, Adelman JP, Maylie J (1997) A human intermediate conductance calcium-activated potassium channel. *Proc Natl Acad Sci USA* **94**: 11651-11656.

Jensen BS, Strobaek D, Christophersen P, Jorgensen TD, Hansen C, Silahtaroglu A, Olesen SP, Ahring PK (1998) Characterization of the cloned human intermediate-conductance Ca²⁺-activated K⁺ channel. *Am J Physiol* **275**: C848-856.

Jiang Y, Lee A, Chen J, Cadene M, Chait BT, MacKinnon R (2002) Crystal structure and mechanism of a calcium-gated potassium channel. *Nature* **417**: 515-522.

Jiang Y, Lee A, Chen J, Ruta V, Cadene M, Chait BT, MacKinnon R (2003) X-ray structure of a voltage-dependent K⁺ channel. *Nature* **423**: 33-41.

MOL #108068

Joiner WJ, Wang LY, Tang MD, Kaczmarek LK (1997) hSK4, a member of a novel subfamily of calcium-activated potassium channels. *Proc Natl Acad Sci USA* **94**: 11013-11018.

Khalili-Araghi F, Jogini V, Yarov-Yarovoy V, Tajkhorshid E, Roux B, Schulten K (2010) Calculation of the gating charge for the Kv1.2 voltage-activated potassium channel. *Biophys J* **98**: 2189-2198.

Klein H, Garneau L, Banderali U, Simoes M, Parent L, Sauve R (2007) Structural determinants of the closed KCa3.1 channel pore in relation to channel gating: results from a substituted cysteine accessibility analysis. *J Gen Physiol* **129**: 299-315.

Kohler R, Wulff H, Eichler I, Kneifel M, Neumann D, Knorr A, Grgic I, Kampfe D, Si H, Wibawa J, Real R, Borner K, Brakemeier S, Orzechowski HD, Reusch HP, Paul M, Chandy KG, Hoyer J (2003). Blockade of the intermediate-conductance calcium-activated potassium channel as a new therapeutic strategy for restenosis. *Circulation* **108**: 1119-1125.

Lemmon G, Meiler J (2013) Towards ligand docking including explicit interface water molecules. *PloS One* **8**: e67536.

Logsdon NJ, Kang J, Togo JA, Christian EP, Aiyar J (1997) A novel gene, hKCa4, encodes the calcium-activated potassium channel in human T lymphocytes. *J Biol Chem* **272**: 32723-32726.

Long SB, Tao X, Campbell EB, MacKinnon R (2007) Atomic structure of a voltage-dependent K⁺ channel in a lipid membrane-like environment. *Nature* **450**: 376-382.

MOL #108068

Maezawa I, Jenkins DP, Jin BE, Wulff H (2012). Microglial KCa3.1 channels as a potential therapeutic target for Alzheimer's disease. *Int J Alzheimers Dis* **2012**: 868972.

Mandell DJ, Coutsias EA, Kortemme T (2009) Sub-angstrom accuracy in protein loop reconstruction by robotics-inspired conformational sampling. *Nat Methods* **6**: 551-552.

McNaughton-Smith GA, Burns JF, Stocker JW, Rigdon GC, Creech C, Arrington S, Shelton T, de Franceschi L (2008) Novel inhibitors of the Gardos channel for the treatment of sickle cell disease. *J Med Chem* **51**: 976-982.

Meiler J, Baker D (2006) ROSETTALIGAND: protein-small molecule docking with full side-chain flexibility. *Proteins* **65**: 538-548.

OEChem, version 1.7.4, OpenEye Scientific Software, Inc., www.eyesopen.com. (2010) Santa Fe, NM, USA.

Pathak MM, Yarov-Yarovoy V, Agarwal G, Roux B, Barth P, Kohout S, Tombola F, Isacoff EY (2007) Closing in on the resting state of the Shaker K⁺ channel. *Neuron* **56**: 124-140.

Pena TL, Rane SG (1999) The fibroblast intermediate-conductance KCa channel, FIK, as a prototype for the cell growth regulatory function of the IK channel family. *J Membr Biol* **172**: 249-257.

Pettersen EF, Goddard TD, Huang CC, Couch GS, Greenblatt DM, Meng EC, Ferrin TE (2004) UCSF Chimera--a visualization system for exploratory research and analysis. *J Comput Chem* **25**: 1605-1612.

MOL #108068

Rauer H, Pennington M, Cahalan M, Chandy KG (1999) Structural conservation of the pores of calcium-activated and voltage-gated potassium channels determined by a sea anemone toxin. *J Biol Chem* **274**: 21885-21892.

Rohl CA, Strauss CE, Misura KM, Baker D (2004) Protein structure prediction using Rosetta. *Methods Enzymol* **383**: 66-93.

Rufo PA, Merlin D, Riegler M, Ferguson-Maltzman MH, Dickinson BL, Brugnara C, Alper SL, Lencer WI (1997) The antifungal antibiotic, clotrimazole, inhibits chloride secretion by human intestinal T84 cells via blockade of distinct basolateral K⁺ conductances. Demonstration of efficacy in intact rabbit colon and in an in vivo mouse model of cholera. *J Clin Invest* **100**: 3111-3120.

Shumilina E, Lam RS, Wolbing F, Matzner N, Zemtsova IM, Sobiesiak M, Mahmud H, Sausbier U, Biedermann T, Ruth P, Sausbier M, Lang F (2008) Blunted IgE-mediated activation of mast cells in mice lacking the Ca²⁺-activated K⁺ channel KCa3.1. *J Immunol* **180**: 8040-8047.

Si H, Heyken WT, Wolfle SE, Tysiac M, Schubert R, Grgic I, Vilianovich L, Giebing G, Maier T, Gross V, Bader M, de Wit C, Hoyer J, Kohler R (2006) Impaired endothelium-derived hyperpolarizing factor-mediated dilations and increased blood pressure in mice deficient of the intermediate-conductance Ca²⁺-activated K⁺ channel. *Circ Res* **99**: 537-544.

Soding J, Biegert A, Lupas AN (2005) The HHpred interactive server for protein homology detection and structure prediction. *Nucleic Acid Res* **33 (Web Server issue)**: W244-248.

MOL #108068

Sprunger LK, Stewig NJ, O'Grady SM (1996) Effects of charybdotoxin on K⁺ channel (KV1.2) deactivation and inactivation kinetics. *Eur J Pharmacol* **314**: 357-364.

Strøbæk D, Brown DT, Jenkins DP, Chen YJ, Coleman N, Ando Y, Chiu P, Jorgensen S, Demnitz J, Wulff H, Christophersen P (2013) NS6180, a new KCa3.1 channel inhibitor prevents T-cell activation and inflammation in a rat model of inflammatory bowel disease. *Br J Pharmacol* **168**: 432-444.

Tang L, El-Din TM, Swanson TM, Pryde DC, Scheuer T, Zheng N, Catterall WA (2016). Structural basis for inhibition of a voltage-gated Ca²⁺ channel by Ca²⁺ antagonist drugs. *Nature* **537**: 117-121.

Tinberg CE, Khare SD, Dou J, Doyle L, Nelson JW, Schena A, Jankowski W, Kalodimos CG, Johnsson K, Stoddard BL, Baker D (2013) Computational design of ligand-binding proteins with high affinity and selectivity. *Nature* **501**: 212-216.

Toyama K, Wulff H, Chandy KG, Azam P, Raman G, Saito T, Fujiwara Y, Mattson DL, Das S, Melvin JE, Pratt PF, Hatoum OA, Gutterman DD, Harder DR, Miura H (2008) The intermediate-conductance calcium-activated potassium channel KCa3.1 contributes to atherogenesis in mice and humans. *J Clin Invest* **118**: 3025-3037.

Tuluc P, Yarov-Yarovoy V, Benedetti B, Flucher BE (2016) Molecular interactions in the voltage sensor controlling gating properties of Ca_v calcium channels. *Structure* **24**: 261-271.

MOL #108068

Urbahns K, Goldmann S, Kruger J, Horvath E, Schuhmacher J, Grosser R, Hinz V, Mauler F (2005) IKCa-channel blockers. Part 2: Discovery of cyclohexadienes. *Bioorg Med Chem Lett* **15**: 401-404.

Urbahns K, Horvath E, Stasch JP, Mauler F (2003). 4-Phenyl-4*H*-pyrans as IK(Ca) channel blockers. *Bioorg Med Chem Lett* **13**: 2637-2639.

Vandorpe DH, Shmukler BE, Jiang L, Lim B, Maylie J, Adelman JP, de Franceschi L, Cappellini MD, Brugnara C, Alper SL (1998) cDNA cloning and functional characterization of the mouse Ca²⁺-gated K⁺ channel, mIK1. Roles in regulatory volume decrease and erythroid differentiation. *J Biol Chem* **273**: 21542-21553.

Wang C, Bradley P, Baker D (2007) Protein-protein docking with backbone flexibility. *J Mol Biol* **373**: 503-519.

Wang J, Yarov-Yarovoy V, Kahn R, Gordon D, Gurevitz M, Scheuer T, Catterall WA (2011). Mapping the receptor site for {alpha}-scorpion toxins on a Na⁺ channel voltage sensor. *Proc Natl Acad Sci USA* **108**: 15426-15431.

Waterhouse AM, Procter JB, Martin DM, Clamp M, Barton GJ (2009) Jalview Version 2-a multiple sequence alignment editor and analysis workbench. *Bioinformatics* **25**: 1189-1191.

Wei AD, Gutman GA, Aldrich R, Chandy KG, Grissmer S, Wulff H (2005) International Union of Pharmacology. LII. Nomenclature and molecular relationships of calcium-activated potassium channels. *Pharmacol Rev* **57**: 463-472.

MOL #108068

Wulff H, Gutman GA, Cahalan MD, Chandy KG (2001) Delineation of the clotrimazole/TRAM-34 binding site on the intermediate conductance calcium-activated potassium channel, IKCa1. *The J Biol Chem* **276**: 32040-32045.

Wulff H, Knaus HG, Pennington M, Chandy KG (2004) K⁺ channel expression during B cell differentiation: implications for immunomodulation and autoimmunity. *J Immunol* **173**: 776-786.

Wulff H, Miller MJ, Hansel W, Grissmer S, Cahalan MD, Chandy KG (2000). Design of a potent and selective inhibitor of the intermediate-conductance Ca²⁺-activated K⁺ channel, IKCa1: a potential immunosuppressant. *Proc Natl Acad Sci USA* **97**: 8151-8156.

Yang F, Vu S, Yarov-Yarovoy V, Zheng J (2016) Rational design and validation of a vanilloid-sensitive TRPV2 ion channel. *Proc Natl Acad Sci USA* **113**: E3657-3666.

Yang F, Xiao X, Cheng W, Yang W, Yu P, Song Z, Yarov-Yarovoy V, Zheng J (2015) Structural mechanism underlying capsaicin binding and activation of the TRPV1 ion channel. *Nat Chem Biol* **11**: 518-524.

Yarov-Yarovoy V, Baker D, Catterall WA (2006a) Voltage sensor conformations in the open and closed states in ROSETTA structural models of K⁺ channels. *Proc Natl Acad Sci USA* **103**: 7292-7297.

Yarov-Yarovoy V, Decaen PG, Westenbroek RE, Pan CY, Scheuer T, Baker D, Catterall WA (2012) Structural basis for gating charge movement in the voltage sensor of a sodium channel. *Proc Natl Acad Sci USA* **109**: E93-E102.

MOL #108068

Yarov-Yarovoy V, Schonbrun J, Baker D (2006b) Multipass membrane protein structure prediction using Rosetta. *Proteins* **62**: 1010-1025.

Zhang JZ, Yarov-Yarovoy V, Scheuer T, Karbat I, Cohen L, Gordon D, Gurevitz M, Catterall WA (2012) Mapping the interaction site for a beta-scorpion toxin in the pore module of domain III of voltage-gated Na⁺ channels. *J Biol Chem* **287**: 30719-30728.

Zhang JZ, Yarov-Yarovoy V, Scheuer T, Karbat I, Cohen L, Gordon D, Gurevitz M, Catterall WA (2011) Structure-function map of the receptor site for beta-scorpion toxins in domain II of voltage-gated sodium channels. *J Biol Chem* **286**: 33641-33651.

Zhou Y, Morais-Cabral JH, Kaufman A, MacKinnon R (2001) Chemistry of ion coordination and hydration revealed by a K⁺ channel-Fab complex at 2.0 Å resolution. *Nature* **414**: 43-48.

MOL #108068

Footnotes

H.W. and V.Y.-Y. are co-senior authors.

This work was supported by startup funds from the University of California and by the CounterACT Program, National Institutes of Health Office of the Director, and the National Institute of Neurological Disorders and Stroke [U54NS079202]. Brandon Pressly was supported by a National Institute of General Medical Sciences funded Pharmacology Training Program [T32GM099608].

Address of persons to receive reprint requests:

- 1) Vladimir Yarov-Yarovoy, Department of Physiology and Membrane Biology, 4131 Tupper Hall, University of California, Davis, Davis, CA 95616; phone: 530-752-5298; email: yarovoy@ucdavis.edu
- 2) Heike Wulff, Department of Pharmacology, Genome and Biomedical Sciences Facility, Room 3502, 451 Health Sciences Drive, University of California, Davis, Davis, CA 95616; phone: 530-754-6136; email: hwulff@ucdavis.edu

MOL #108068

Figure Legends

Fig. 1. Sequence alignment between the KCa3.1, Kv2.1 and KcsA channel pore-forming domains. Transmembrane regions S5 and S6 and the pore P-helix are underlined by black bars and labeled. Positions of residues forming a part of drug receptor sites discussed in this paper are marked and labeled. Amino acids were colored with Jalview program (Clamp et al., 2004; Clamp, 1999; Waterhouse et al., 2009) using the Zappo color scheme, where hydrophobic residues (I, L, V, A, and M) are colored pink, aromatic residues (F, W, and Y) are colored orange, positively charged residues (K, R, and H) are colored blue, negatively charged residues (D and E) are colored red, hydrophilic residues (S, T, N, and Q) are colored green, P and G colored magenta, and C is colored yellow.

Fig. 2. Kv1.2 based homology model of the KCa3.1 channel pore-forming domain. A, View of the ribbon representation of the homology model of the KCa3.1 channel pore-forming domain from the extracellular side of the membrane. Each subunit is colored individually. Side chains are shown in stick representation. B, View of the model shown in panel A from the intracellular side of the membrane. C, Transmembrane view of the model shown in panel A. D, Surface representation of the transmembrane view of the model shown in panel A. The pore has been sliced in the middle to highlight the pore lumen and fenestration regions of the structure.

Fig. 3. KcsA-based homology model of the KCa3.1 channel pore-forming domain and comparison of the TRAM-34 position in the KcsA- and the Kv1.2-based models. A, View of the ribbon representation of the homology model of the KCa3.1 channel pore-forming domain from the extracellular side of the membrane. Each subunit is colored individually. B Transmembrane view of the model shown in panel A. C, Surface representations of the transmembrane views of

MOL #108068

TRAM-34 (black) energy minimized in the KcsA- and the Kv1.2-based model. The pore has been sliced in the middle to highlight the pore lumen and fenestration regions of the structure.

Fig. 4. TRAM-34 interaction with the KCa3.1 channel pore. A, Transmembrane view of the ribbon representation of one of the lowest energy models of the KCa3.1 channel complex with TRAM-34. Only 3 subunits are shown for clarity and each subunit is colored individually. Side chains of T250 and V275 are shown in space-filling representation and labeled. TRAM-34 is shown in ball and stick representation with a transparent molecular surface. Transmembrane segments S5 and S6 are labeled for one of the subunits. B, Intracellular view of the model shown in panel A with all 4 subunits shown. C, Close-up of the transmembrane model shown in panel A. D, Surface representation of the transmembrane view of the model shown in panel A. Only 3 subunits are shown for clarity. T250 and V275 side chain atoms are colored light gray (carbon), white (hydrogen), and red (oxygen). TRAM-34 is colored green.

Fig. 5. Interaction of several TRAM-34 derivatives with the KCa3.1 channel pore. A, Transmembrane view of the ribbon representation of one of the lowest energy models of the KCa3.1 channel complex with senicapoc. Only 3 subunits are shown for clarity and each subunit is colored individually. T250 and V275 side chain atoms are colored light gray (carbon), white (hydrogen), and red (oxygen). Senicapoc is shown in stick representation with a transparent molecular surface. Hydrogen bonds are shown in pink. B, Overlay of the lowest energy TRAM-34 (black) and senicapoc (orange) models. Hydrogen bonds between the NH₂ group of senicapoc and two T250 residues are shown in pink. The hydrogen bond between one T250 residue and the pyrazole ring of TRAM-34 is shown in green. C, Representative binding pose of TRAM-7 (shown in stick presentation with a transparent molecular surface). D, One of two dominant binding poses of TRAM-11. E, Structures of TRAM-34, senicapoc, TRAM-11, TRAM-7, TRAM-18 and TRAM-19.

MOL #108068

Fig. 6. NS6180 interaction with the KCa3.1 channel pore. A, Transmembrane view of the ribbon representation of one of the lowest energy models of the KCa3.1 channel complex with NS6180. Only 3 subunits are shown for clarity and each subunit is colored individually. Side chains of T250 and V275 are shown in space-filling representation and labeled. NS6180 is shown in stick representation with a transparent molecular surface. Transmembrane segments S5 and S6 are labeled for one of the subunits. B, Intracellular view of the model shown in panel A with all 4 subunits shown. C, Close-up of the transmembrane view of the model shown in panel A. D, Surface representation of the transmembrane view of the model shown in panel A. Only 3 subunits are shown for clarity. T250 and V275 side chain atoms are colored light gray (carbon), white (hydrogen), and red (oxygen). NS6180 is colored green.

Fig. 7. Nifedipine interaction with the KCa3.1 channel pore. A, Transmembrane view of the ribbon representation of one of the lowest energy models of the KCa3.1 channel complex with nifedipine. Only 2 adjacent subunits are shown for clarity and each subunit is colored individually. Side chains of T212 and V272 are shown in space-filling representation and labeled. Nifedipine is shown in stick representation with a transparent molecular surface. Transmembrane segments S5 and S6 are labeled for one of the subunits. B, Intracellular view of the model shown in panel A with all 4 subunits shown. C, Close-up and 90° rotated transmembrane view of the model shown in panel B with only 2 subunits shown. Hydrogen bonds are shown in green. D, Surface representation of the transmembrane view of the model shown in panel B. All 4 subunits are shown. Nifedipine is colored green. E, Concentration-dependent inhibition of WT and mutant KCa3.1 channels by nifedipine. WT KCa3.1 channels are inhibited by nifedipine with an IC_{50} concentration of $0.74 \pm 0.18 \mu\text{M}$ ($h = 0.82 \pm 0.28$; $n = 5$). While the fenestration mutants T212F ($IC_{50} = 2.70 \pm 1.98 \mu\text{M}$; $h = 0.71 \pm 0.14$; $n = 11$), V272F ($IC_{50} = 5.86 \pm 2.12 \mu\text{M}$; $h = 0.75 \pm 0.06$; $n = 4$) and T212F-V272F ($10.28 \pm 5.18 \mu\text{M}$; $h = 1.38 \pm$

MOL #108068

0.58; $n = 12$) decrease nifedipine block by 4, 8, and 14-fold, respectively, the pore double mutant T250S-V275A ($IC_{50} = 0.16 \pm 0.15 \mu\text{M}$; $h = 0.73 \pm 0.26$; $n = 4$) does not reduce nifedipine block. F-H, Individual current traces showing inhibition of KCa3.1 currents in the presence 1 μM and 10 μM nifedipine. I, Concentration-dependent relationship of inhibition for the fenestration mutants by TRAM-34 demonstrating the lack of an effect of the fenestration mutants on the action of this pore-selective blocker: T212F ($IC_{50} = 29.0 \pm 14.5 \text{ nM}$; $h = 0.76 \pm 0.26$; $n = 5$), V272F ($IC_{50} = 23.0 \pm 11.5 \text{ nM}$; $h = 0.64 \pm 0.13$; $n = 4$) and T212F-V272F ($IC_{50} = 28.5 \pm 6.3 \text{ nM}$; $h = 0.89 \pm 0.11$; $n = 6$). Data points are expressed as mean \pm SD; $n =$ number of independent cells used for constructing the concentration response curves.

Fig. 8. (S)-4-Phenyl-pyran interaction with KCa3.1 channel pore. A, Transmembrane view of the ribbon representation of one of the lowest energy models of the KCa3.1 channel complex with (S)-4-phenyl-pyran (shown in stick representation with a transparent molecular surface). Only 3 subunits are shown for clarity and each subunit is colored individually. Side chains of T250, V275, and T278 are shown in space-filling representation and labeled. Transmembrane segments S5 and S6 are labeled for one of the subunits. B, Intracellular view of the model shown in panel A with all 4 subunits shown. C, Close-up of the transmembrane view shown in panel A. D, Surface representation of the transmembrane view of the model shown in panel A. Only 3 subunits are shown for clarity. T250, V275, and T278 side chain atoms are colored light gray (carbon), white (hydrogen), and red (oxygen). S-4-phenyl-pyran is colored green. E, Concentration-dependent inhibition of WT and mutant KCa3.1 channels by 4-phenyl-pyran. WT KCa3.1 is inhibited by 4-phenyl-pyran with an IC_{50} of $7.7 \pm 4.5 \text{ nM}$ ($h = 1.20 \pm 0.27$; $n = 5$). While the pore mutants T250S ($IC_{50} = 969.9 \pm 242.7 \text{ nM}$; $h = 0.61 \pm 0.16$; $n = 3$), T250S-V275A ($IC_{50} = 4.45 \pm 1.63 \mu\text{M}$; $h = 1.02 \pm 0.36$; $n = 7$) and T278F ($IC_{50} = 321.04 \pm 130.82 \text{ nM}$; $h = 0.97 \pm 0.38$; $n = 11$) decrease 4-phenyl-pyran block by 125, 575 and 40-fold, respectively, neither of the fenestration mutants V272F ($IC_{50} = 30.1 \pm 2.4 \text{ nM}$; $h = 1.65 \pm 0.48$; $n = 3$) or T212F-V272F (IC_{50}

MOL #108068

= 30.2 ± 4.5 nM; $h = 1.54 \pm 0.25$; $n = 5$) significantly reduce 4-phenyl-pyran block. Data points are expressed as mean \pm SD; n = number of independent cells used for constructing the concentration response curves. F-H, Current traces showing examples of inhibition of WT KCa3.1, T212-V272F and T250S-T275A currents by 4-phenyl-pyran.

Fig. 9. (*R*)-4-Phenyl-pyran interaction with KCa3.1 channel pore. A, Transmembrane view of the ribbon representation of one of the lowest energy models of the KCa3.1 channel complex with (*R*)-4-phenyl-pyran (shown in stick representation). Only 3 subunits are shown for clarity and each subunit is colored individually. Side chains of T250, V275, and T278 are shown in space-filling representation and labeled. Hydrogen bonds are shown in pink. B, Close up view of the model shown in panel A.

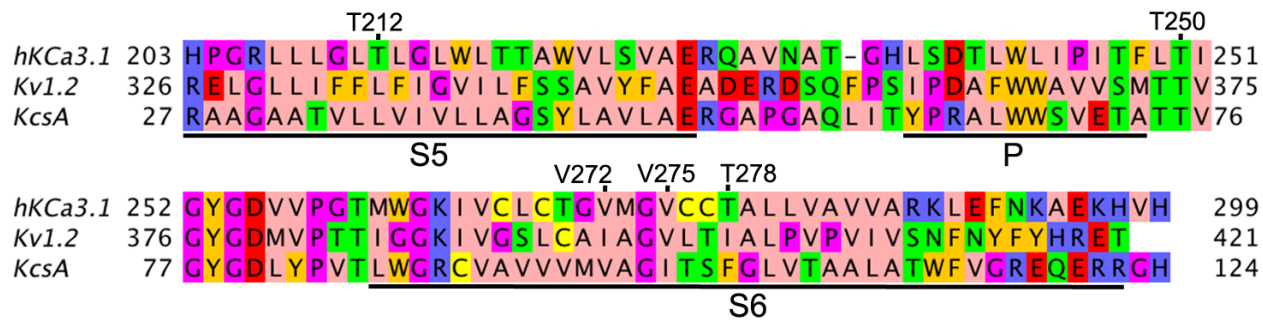


Figure 1

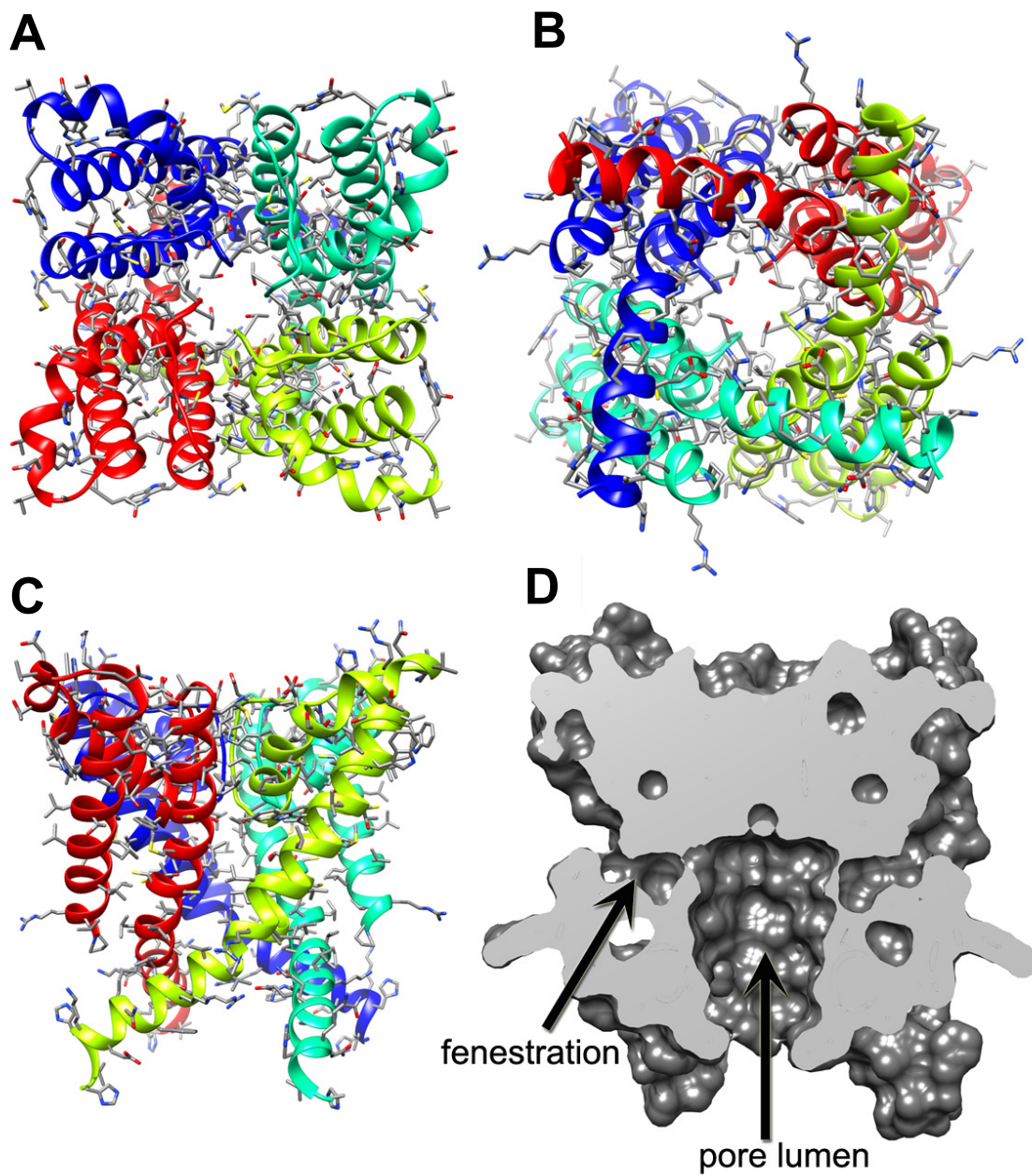


Figure 2

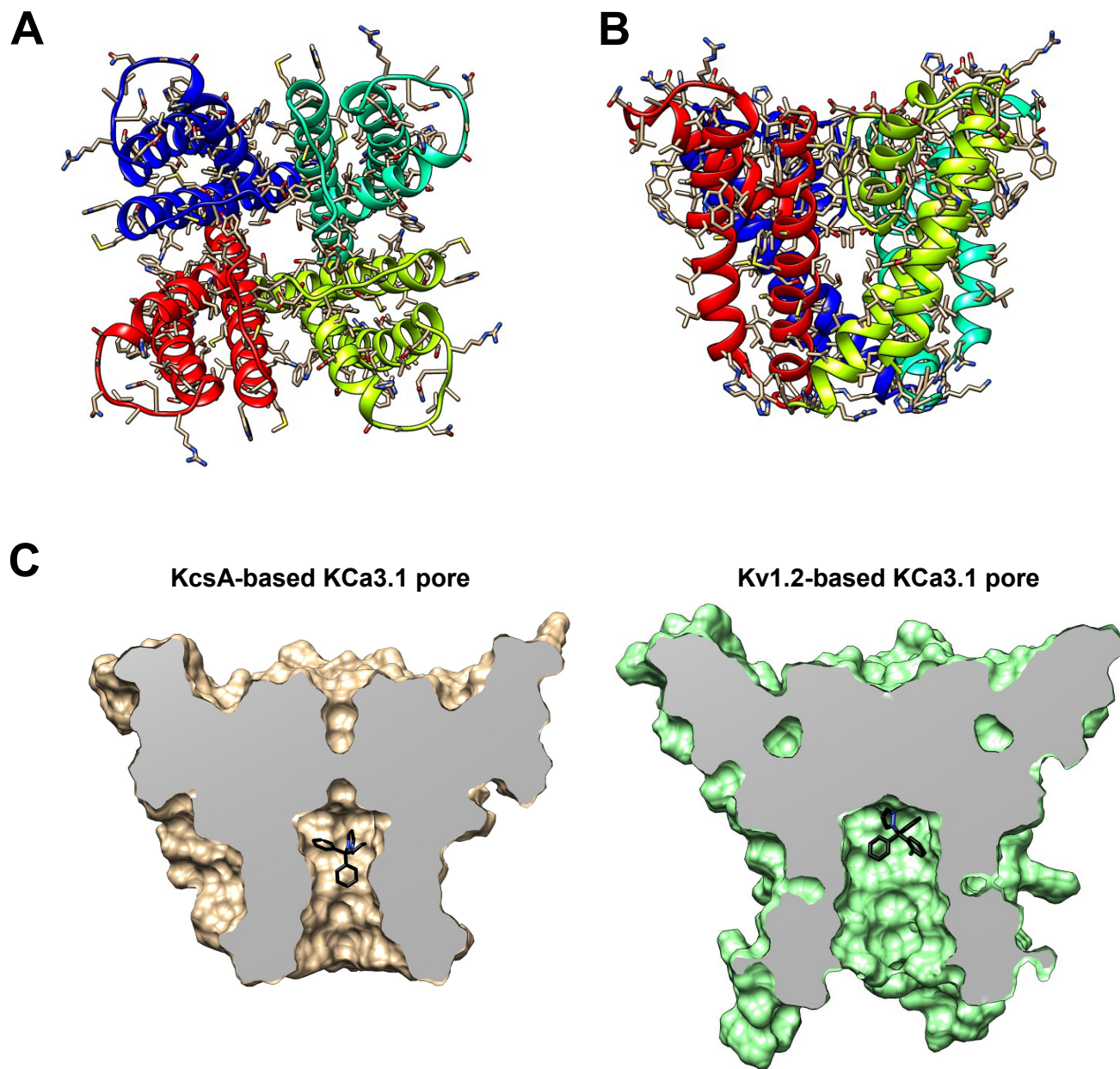


Figure 3

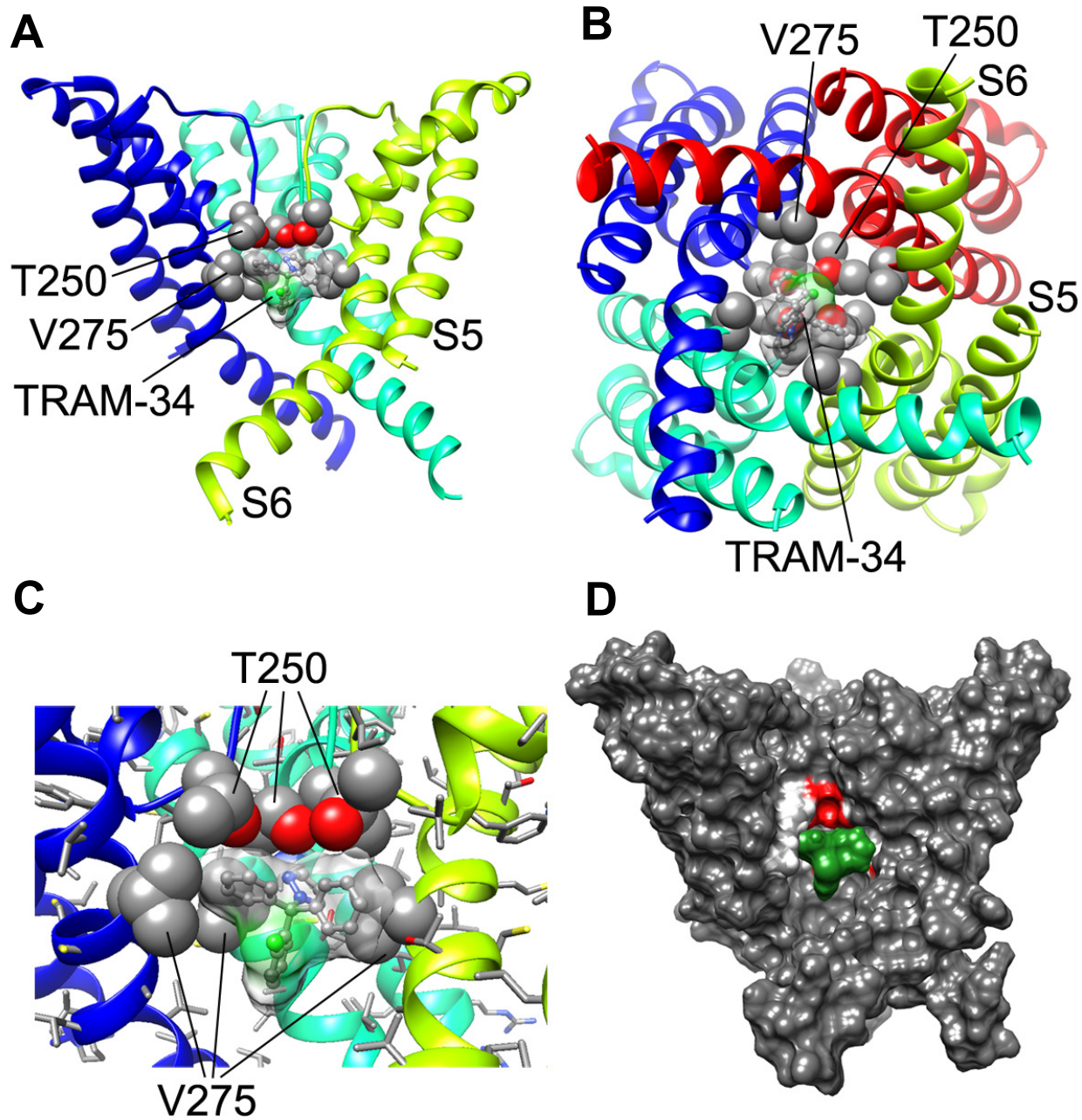


Figure 4

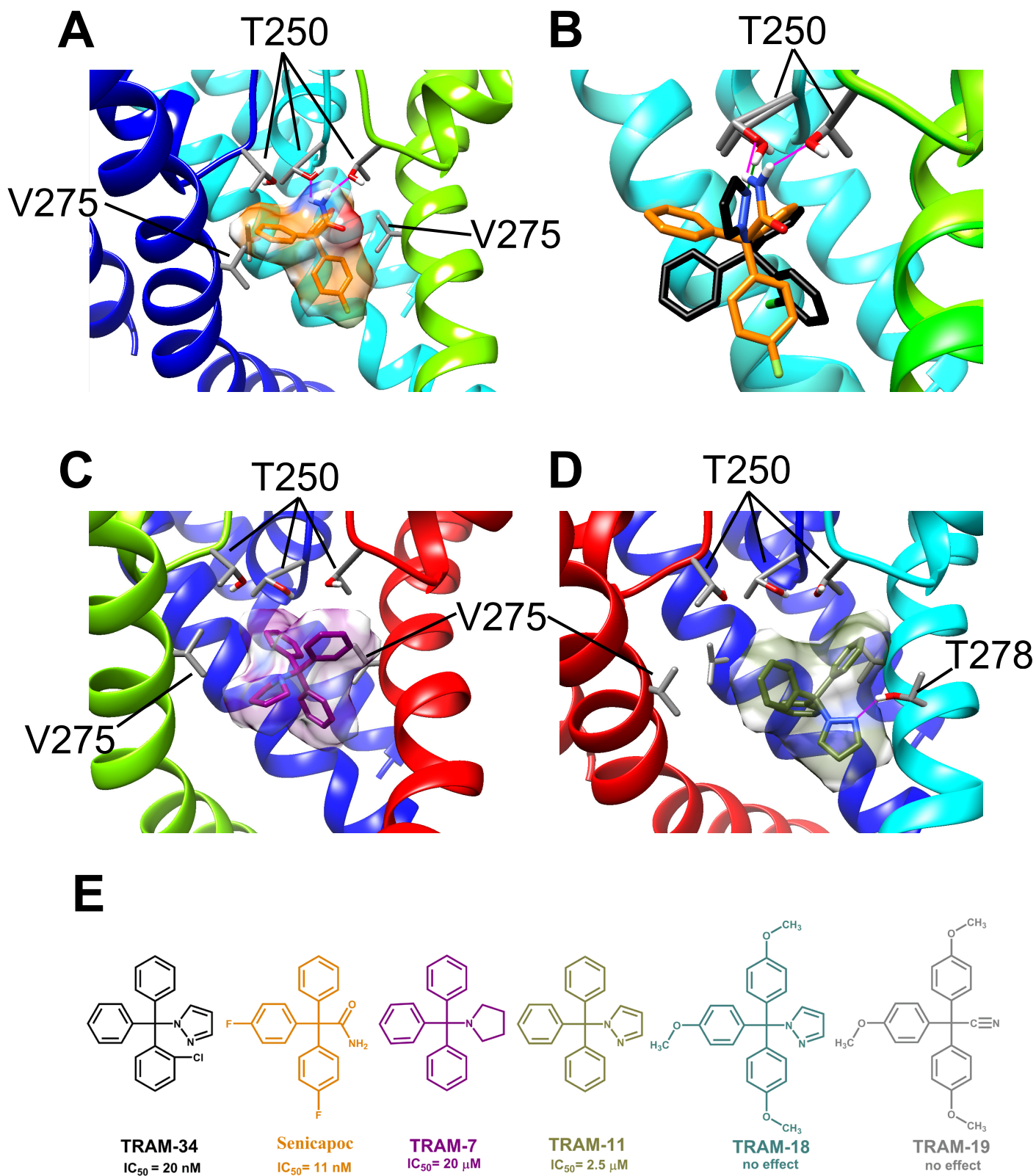


Figure 5

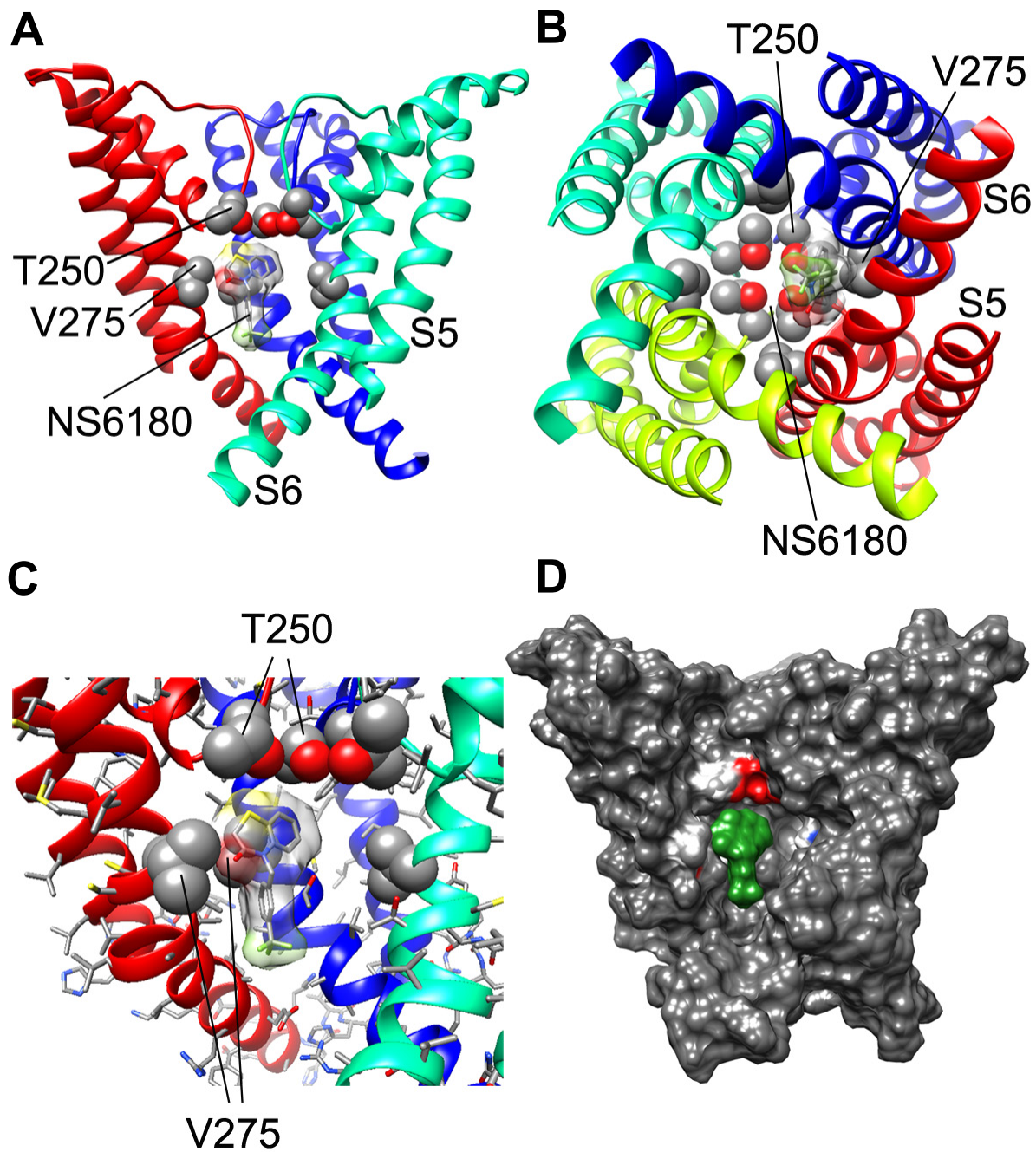


Figure 6

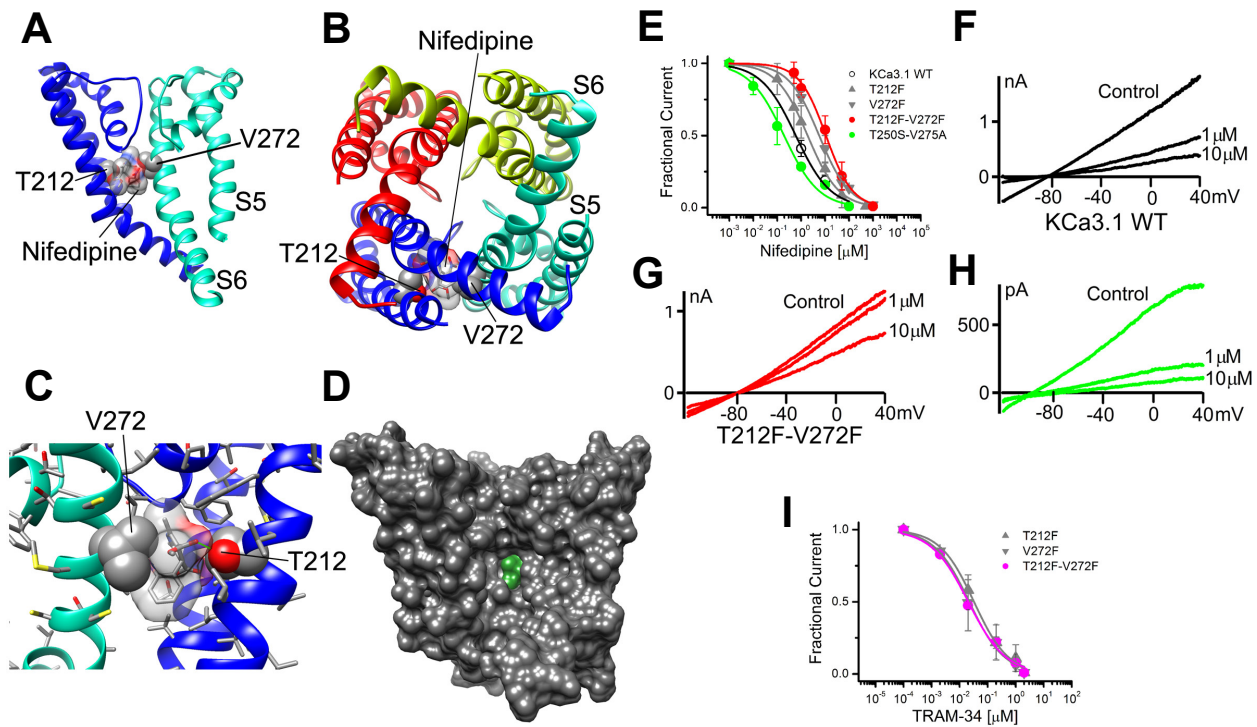


Figure 7

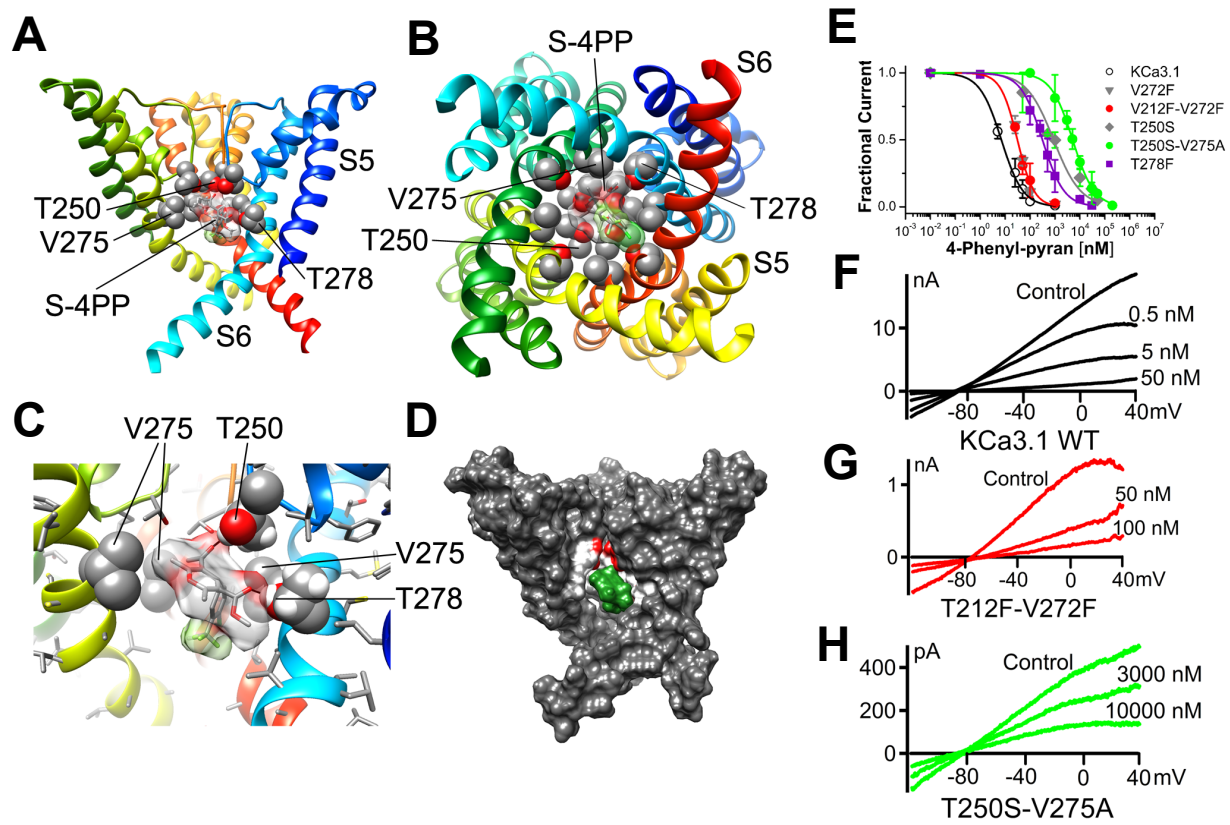


Figure 8

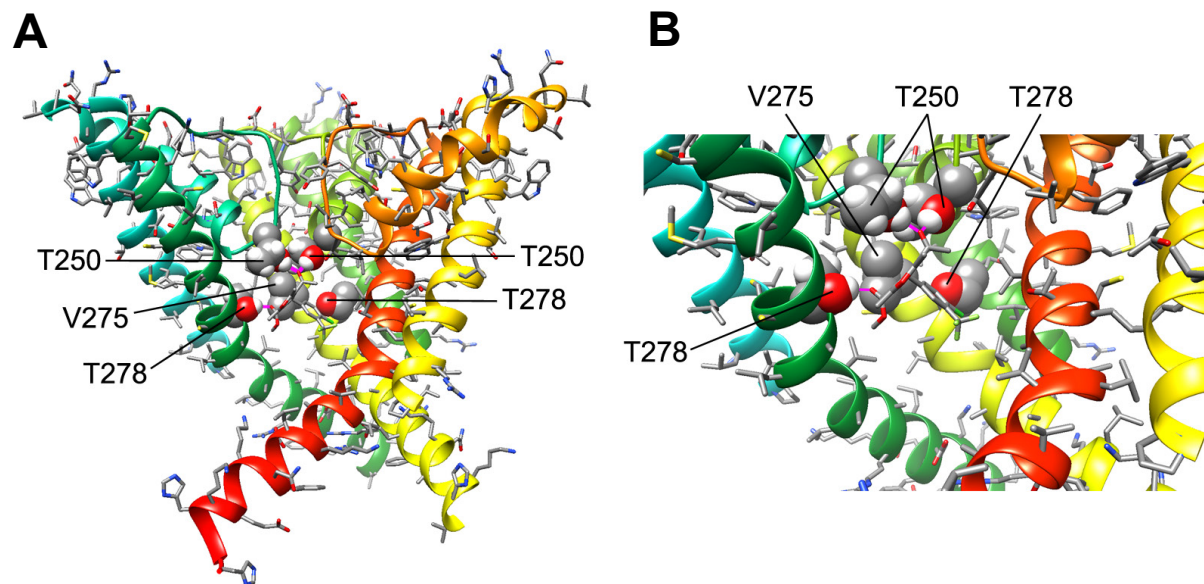


Figure 9

Supplemental Data for *Molecular Pharmacology* article:

Title: Structural Insights into the Atomistic Mechanisms of Action of Small Molecule Inhibitors Targeting the KCa3.1 Channel Pore

Authors: Hai M. Nguyen, Vikrant Singh, Brandon Pressly, David Paul Jenkins, Heike Wulff, Vladimir Yarov-Yarovoy

Journal Title: *Molecular Pharmacology*

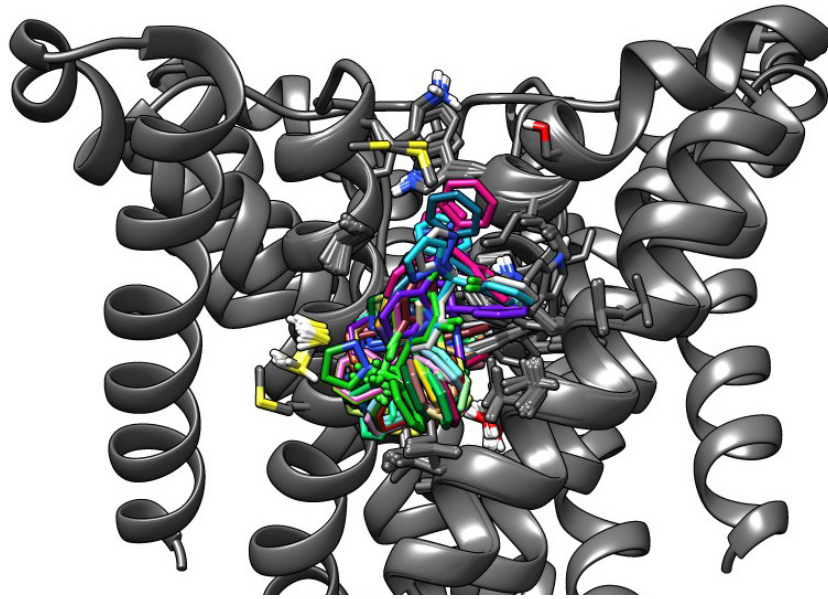
This file contains:

1 Supplemental Figure of the Kv1.2-based KCa3.1 pore model showing TRAM-34 docked into the fenestration region where it fails to converge on an energetically favorable binding pose

1 Supplemental Figure of the KcsA-based KCa3.1 pore model showing that TRAM-34 fails to converge on an energetically favorable binding pose when docked in the inner pore

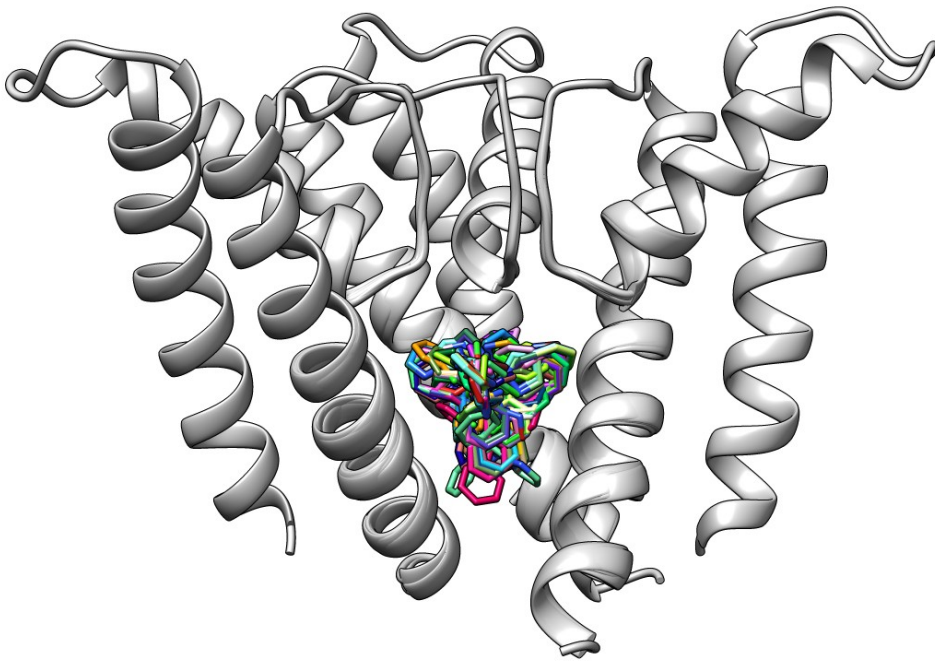
1 Supplemental Figure showing the results of the electrophysiological testing of TRAM-11 on the KCa3.1-T278F mutant and a model of TRAM-11 docked into the KCa3.1-T278F pore

Description of the synthesis and physical data for methyl-5-acetyl-4-(4-chloro-3-(trifluoromethyl)phenyl)-2,6-dimethyl-4*H*-pyran-3-carboxylate



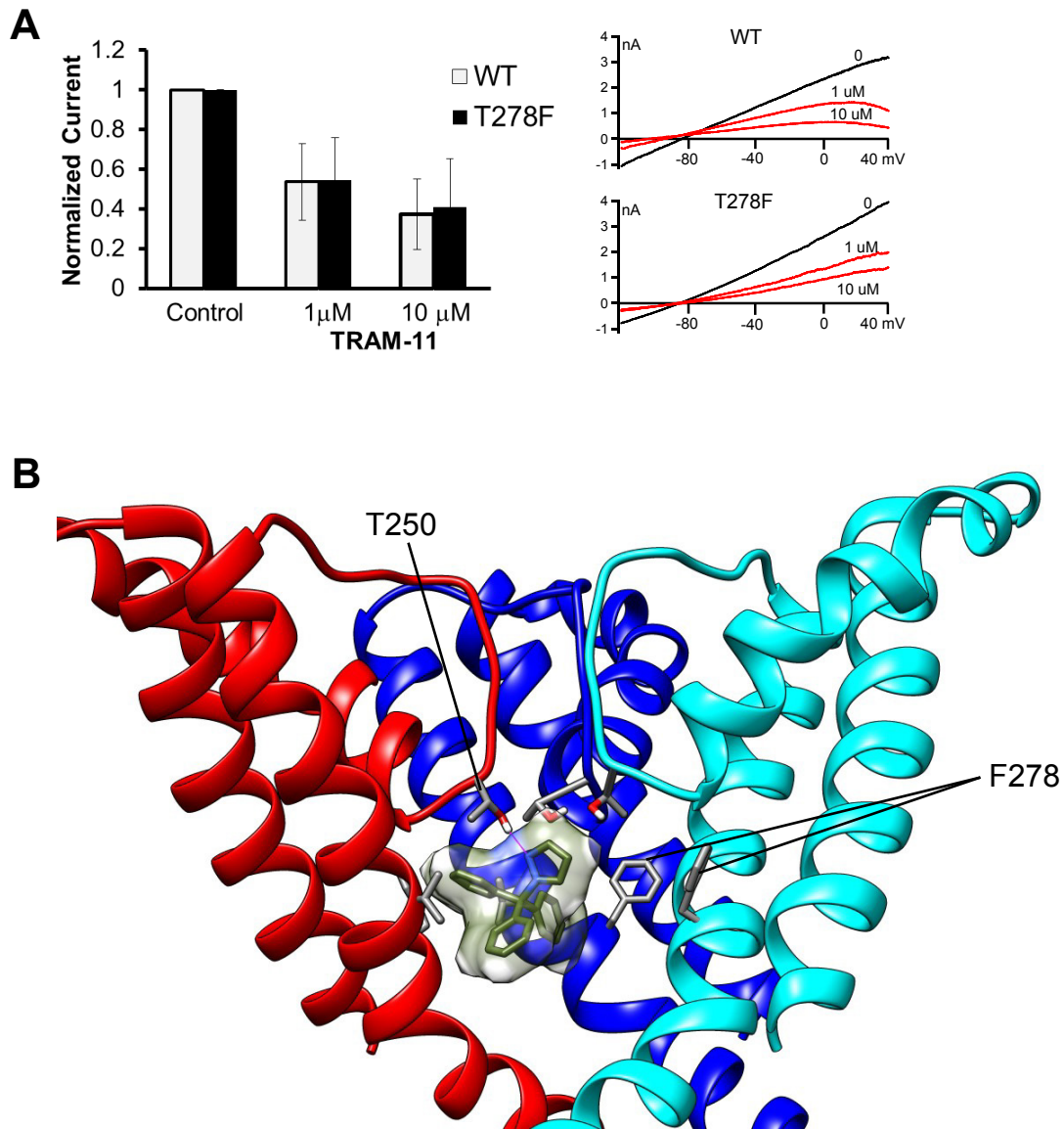
Supplemental Figure 1:

TRAM-34 docked into the fenestration region of the Kv1.2-based KCa3.1 model. None of the top 50 models with the lowest binding score converge.



Supplemental Figure 2:

TRAM-34 docked into inner pore of the KcsA-based KCa3.1 model. None of the top 50 models with the lowest binding score converge.

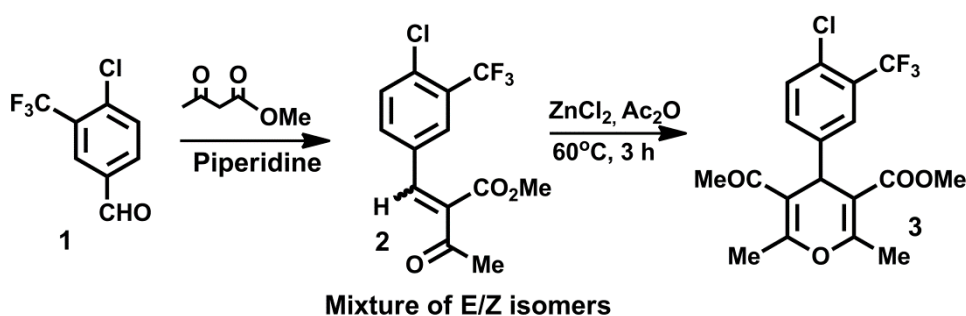


Supplemental Figure 3:

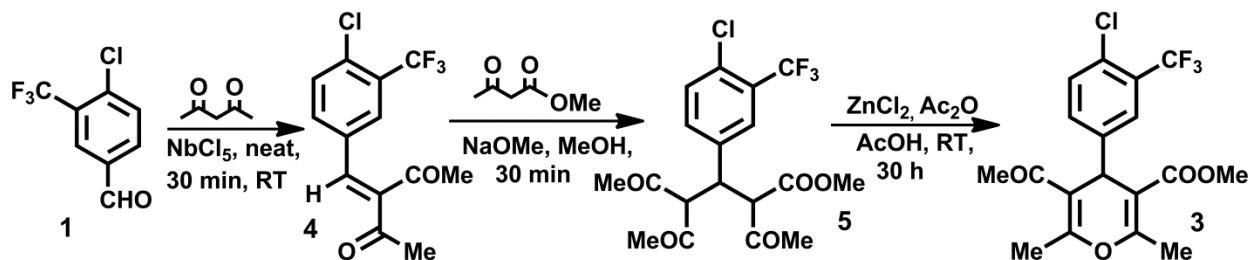
A, TRAM-11 inhibits WT KCa3.1 and the T278F mutant with equal potency ($n = 3$). B, Dominant binding pose of TRAM-11 in the model of the Kv1.2-based KCa3.1-T278F mutant channel. Instead of forming a hydrogen bond with T278 TRAM-11 has “moved up” and is now forming a hydrogen bond with T250.

Synthesis of an exemplary 4-phenyl-pyran (Methyl-5-acetyl-4-(4-chloro-3-(trifluoromethyl)phenyl)-2,6-dimethyl-4H-pyran-3-carboxylate (3).

We resynthesized an exemplary 4-phenyl-pyran from the Bayer KCa3.1 work (Urbahns et al., 2003). Unfortunately, the original procedure (Scheme 1) reported for 4-phenyl-pyran (methyl-5-acetyl-4-(4-chloro-3-(trifluoromethyl)phenyl)-2,6-dimethyl-4H-pyran-3-carboxylate (3), which is compound *rac*-11 in Urbahns *et al.* (Urbahns et al., 2003) and the accompanying patent (Urbahns and Mauler, 1997), proved inefficient in our hands. The first synthetic step, a piperidine mediated Knoevenagel condensation between aldehyde 1 and methyl acetoacetate furnished a very low yield of a mixture of the two geometrical isomers of 2, while the second step did not yield any desired product in our hands. Thus, we adopted an entirely different, Lewis acid catalyzed approach (Scheme 2) for the first step and obtained product 4 in high yield using easily available and inexpensive starting materials and reagents. For the final product we undertook a two-step route consisting of a base catalyzed Michael reaction followed by acid catalyzed pyran ring formation. This alternative strategy furnished the desired product 3 at the end of the sequence with an 18% overall yield.



Scheme 1: Synthetic route for the synthesis of 3 reported by Urbahns *et al.* (Urbahns et al., 2003)



Scheme 2: Modified strategy adopted for the synthesis of **3**.

Experimental Procedures:

Chemical synthesis of methyl-5-acetyl-4-(4-chloro-3-(trifluoromethyl)phenyl)-2,6-dimethyl-4H-pyran-3-carboxylate (= 4-Phenylpyran). All starting materials and solvents were purchased as ACS grade or the highest available purity from Sigma-Aldrich unless specifically stated.

3-(4-Chloro-3-(trifluoromethyl)benzylidene)pentane-2,4-dione (4): Compound (**1**), 4-chloro-3-(trifluoromethyl)benzaldehyde (98% purity), was purchased from Synquest Laboratories (Alachua, FL). Solid niobium chloride (500 mg) was added to a mixture of aldehyde (**1**) (2.3 g, 11.03 mM) and acetyl acetone (1.1 g, 11.03 mM) placed in a 20 mL flask. After about 30 min the resultant solid mixture was dissolved in 25 mL chloroform and was washed with saturated sodium bicarbonate solution. The organic phase was dried over anhydrous sodium sulfate and the solvent was removed under reduced pressure. Crude product was recrystallized from a dichloromethane/cyclohexane (1:1) mixture, yielding 2.4 g (75%) of compound **4** as a light yellow crystalline solid. M.p. 85.5-86.2°C; ¹H-NMR (800 MHz, DMSO-d₆): δ = 8.03 (d, 1 H, *J* = 1.90 Hz), 7.86 (d, 1 H, *J* = 8.40 Hz), 7.84 (s, 1 H), 7.71 (dd, 1 H, *J*₁ = 1.90 Hz, *J*₂ = 8.40 Hz), 2.49 (s, 3 H), 2.31 (s, 3 H). ¹³C-NMR (200 MHz, DMSO-d₆): δ = 26.3, 31.4, 122.5 (q, *J* = 271.6 Hz), 127.1 (q, *J* = 30.7 Hz), 129.2 (q, *J* = 5.2 Hz), 132.3, 132.4, 132.8, 134.1, 137.2, 143.9, 197.8, 205.0.

Methyl-2,4-diacetyl-3-(4-chloro-3-(trifluoromethyl)phenyl)-5-oxohexanoate (5). To a suspension of sodium methoxide (162 mg, 3 mM) in 10 ml dry methanol, placed in a 50 mL flask was added methyl acetoacetate (357 mg, 3 mM) at 0°C. The resulting mixture was allowed to warm to room temperature followed by addition (over 3 min) of 581 mg (2 mM) Michael acceptor (4), dissolved in 3 mL of dry THF. After 30 minutes, 0.5 mL acetic acid was added to the reaction mix and methanol was evaporated under vacuum. 1 g of crude product (5) thus obtained was immediately used for the next step.

Methyl-5-acetyl-4-(4-chloro-3-(trifluoromethyl)phenyl)-2,6-dimethyl-4H-pyran-3-carboxylate (3). The crude product (5) from the previous step (1 g) was slowly added to a stirred mixture of zinc chloride (600 mg), acetic acid (1.5 mL) and acetic anhydride (2.0 mL). After about 30 h, water (10 mL) was added and the resulting mixture was extracted with diethyl ether. The organic phase was washed with saturated sodium bicarbonate solution, dried over anhydrous sodium sulfate, and the solvent removed under reduced pressure. Crude product (800 mg) was purified by successive column and preparative thin layer chromatography using an ethylacetate:hexane (15:85) mixture to furnish 140 mg (18% over two steps) of compound 3 as a colorless liquid. ¹H-NMR (800 MHz, DMSO-d₆): δ = 2.20 (s, 3H) 2.35-2.36 (two merged s, 6H); 3.69 (s, 3H); 4.84 (s, 1H); 7.35 (d, 1H, J = 8.3 Hz); 7.38 (d, 1H, J = 8.3 Hz); 7.53 (s, 1H). ¹³C-NMR (200 MHz, DMSO-d₆): δ = 19.0, 19.6, 30.5, 38.4, 51.8, 107.9, 115.9, 122.9 (q, J = 271.6 Hz), 127.4 (q, J = 5.2 Hz), 128.4 (q, J = 31.0 Hz), 130.8, 131.6, 132.9, 144.1, 158.2, 159.4, 166.8, 197.8. HRMS (ESI): m/z calculated for C₁₈H₁₆ClF₃O₄ (M + H)⁺: 389.0756, found: 389.0767.

References

Urbahns K, Horvath E, Stasch JP and Mauler F (2003) 4-Phenyl-4H-pyrans as IK(Ca) channel blockers. *Bioorg & Med Chem Lett* **13**:2637-2639.

Urbahns K and Mauler F (1997) EP 0758648 *Chem Abstr* 247810